creative commons
COMMONS DEED

저작자표시-비영리-변경금지 2.0 대한민국

이용자는 아래의 조건을 따르는 경우에 한하여 자유롭게

- 이 저작물을 복제, 배포, 전송, 전시, 공연 및 방송할 수 있습니다.

다음과 같은 조건을 따라야 합니다:

**저작자표시**. 귀하는 원저작자를 표시하여야 합니다.

**비영리**. 귀하는 이 저작물을 영리 목적으로 이용할 수 없습니다.

**변경금지**. 귀하는 이 저작물을 개작, 변형 또는 가공할 수 없습니다.

- 귀하는, 이 저작물의 재이용이나 배포의 경우, 이 저작물에 적용된 이용허락조건을 명확하게 나타내어야 합니다.
- 저작권자로부터 별도의 허가를 받으면 이러한 조건들은 적용되지 않습니다.

**저작권법에 따른 이용자의 권리는 위의 내용에 의하여 영향을 받지 않습니다.**

이것은 이용허락규약(Legal Code)을 이해하기 쉽게 요약한 것입니다.

Disclaimer

dCollection

공학박사 학위논문

# Configuration-specific hysteresis model for Tendon-Sheath Mechanism

## 형태적응형 이력현상 모형을 이용한 유연구동 메커니즘의 모델링

2020년 8월

서울대학교 대학원

기계항공공학부

김 홍 민

# Abstract

Flexible surgical robots and instruments are slowly paving its way into the modern surgical arena. Compared to conventional laparoscopic surgical systems, flexible systems have some distinct advantages in that it can approach surgical targets that were unreachable before, leaves less scar and therefore reducing recovery time for patients.

In order to drive the articulated surgical instrument's joints, flexible instruments require a tendon-sheath mechanism (TSM). Utilization of TSM brings about a different attribute in a position control standpoint, compared to the rather simple cable-pulley system found in conventional robotic surgical instruments.

In this research, a tendon-sheath mechanism was configured, taking into account the actual size constraint of a robotic surgical instrument and the material characteristics of the components. An experiment hardware was designed to measure the input signal and the corresponding output response while varying the shape configuration parameters of TSM. Twenty four distinct experiments with different shape configuration parameters were carried out to identify how the shape affects the performance and the hysteresis curve of the TSM.

For modeling the hysteretic behavior of the TSM, a composite model consisting of elementary hysteresis operators is proposed. Such a composite model's parameters are empirically identified with least-squares optimization, for every shape configurations defined. The model processes the input to produce an estimated output for a certain shape, and this was verified with various types of input signals.

Lastly, for compensating TSM's hysteretic behavior, a recursive algorithm producing inverse control signal from the empirical model is proposed, with a guaranteed real-time performance. The inverse algorithm's position control effectiveness was verified under various shape configurations and input signal types.

**Keyword :** surgical robotics, surgical instruments, tendon-sheath mechanism, hysteresis, position control.

**Student Number :** 2015-30165

# Table of Contents

# List of the Tables

# List of the Figures

# Chapter 1. Introduction

## 1.1 Background

### 1.1.1 Evolution of surgical robotics

The first reported use of robotic technology in any surgical procedure dates back to 1985 [1], which uses a PUMA (Programmable Universal Machine for Assembly) 560 robot to perform a CT-guided biopsy. Since then, many trials utilizing computerized numerical control technologies and robotics were carried out in various surgical settings, but many of which focused on the passive aspect of a surgical procedure such as preoperative planning, precision measurement, assisting simple repetitive tasks, etc. [2]. In the mid-1990s, robotic system that focused on teleoperation performing surgery in a remote setting [3] [4], the first FDA approved robotic system to perform abdominal surgical procedures [5] was developed and proved the feasibility and showed distinct advantages over conventional surgery techniques when using a robotic system: steady surgical field and higher accuracy that helped to perform more complex procedures [2]

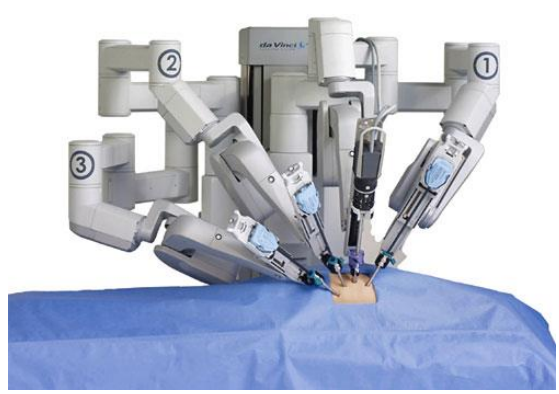


Fig 1.1 da Vinci S system with 4 laparoscopic robotic instruments [6]

From the late-1990s the ZEUS platform (Computer Motion Inc.) and da Vinci

platform (Intuitive Surgical Inc.) have been competing against each other, pushing the boundaries of robotic laparoscopic surgery until the two companies merged in 2003 [7]. Innovation and enhancements were centered on the da Vinci platform, and it dominated the robotic surgery market for almost a decade, until recently several companies emerged as a competition to the market leader [8]. Intuitive Surgical Inc. first introduced the da Vinci S system in 2006, a 4-arm laparoscopic robotic platform. (Fig. 1.1) The next generation models, da Vinci Si and da Vinci Xi that were introduced in 2009 and 2014 respectively, were embodiments of constant enhancements of surgical capabilities and imaging systems but were mainly focused on the same surgical procedure: multi-port larparoscopic surgery. In 2011, Intuitive Surgical developed a single-site surgical instrument that were usable in da Vinci Si at the time, and in 2018, da Vinci SP, a single-port 4-arm system was unveiled. In the recent years, many research groups and companies are heading towards single incision robotic platforms for a truly minimally invasive surgery.

Fig 1.2 da Vinci SP system – Single port, 4-arm [9]

### 1.1.2 Flexible robotic systems

As the laparoscopic robotic systems such as da Vinci platform continued its way into minimally invasive surgical procedures, one of the major driving factors for innovation in surgical robotics was implementing a flexible robotic platform. One of the more established side of thoughts was the NOTES (Natural Orifice Transluminal Endoscopic Surgery) which approaches the surgical target through the natural orifices of the body, such as oral cavity and rectum. In the recent years, there are many attempts applying flexible robotic systems in various settings, aside from NOTES such as in single-port laparoscopic surgery, neurosurgery, and ear-nose-throat surgery. The advantages of using flexible systems rather than the conventional rigid type robotic platforms are that due to the inherent flexibility of the robot, it can adapt passively to various obstacles, provide better imaging in tight spaces and the ability to access remote targets with a single incision or entry point.

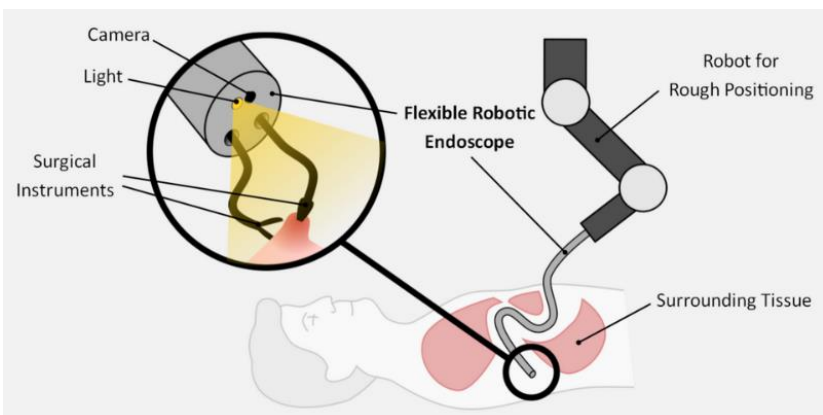


Fig. 1.3 Conceptual drawing of flexible robotic system [10]

The detailed structure of flexible robotic systems varies by case to case, but in general they share similar configuration. Most systems consist of flexible global positioning device that macroscopically place the flexible surgical instruments near the surgical target, such as shown in Fig 1.3. Given the size constraint of endoscopic

surgical procedures, usually 2 surgical instruments are guided by this global positioning device. The surgical instruments may be placed internally within this global positioning device in which case this is called an overtube (Fig. 1.4) or a guide tube (Fig. 1.5). Such tube is almost identical to a commercial endoscope equipped with an imaging system, light source, and in some cases with suction and irrigation ports. In some other instances, a smaller endoscope with camera and light source would be inserted in to one of the three channels of an overtube instead of the imaging system being integrated with itself. In the other category, there are systems that employ a backbone-like element that externally holds the surgical instruments, as shown in Fig 1.6, which guide the instruments globally to the surgical site. The backbone element is usually integrated with an imaging system and light source. For both cases, global positioning device may be robotically driven or manually operated, and once it reaches the surgical target it serves as a local fixture for the surgical instruments. There are many research, developments and concepts that are being tested on the flexible surgical robots but as of 2020, none of the systems are commercially available. There are many technical challenges yet to be overcome, and one of the issues, being precise position control will be of focus of this research.

Fig 1.4 Endoluminal surgical system; Two flexible surgical instruments guided internally, by two channels inside an overtube. Another channel is dedicated for imaging device, and a small independent channel for irrigation. An overtube is manually operated to roughly reach the target surgery site.

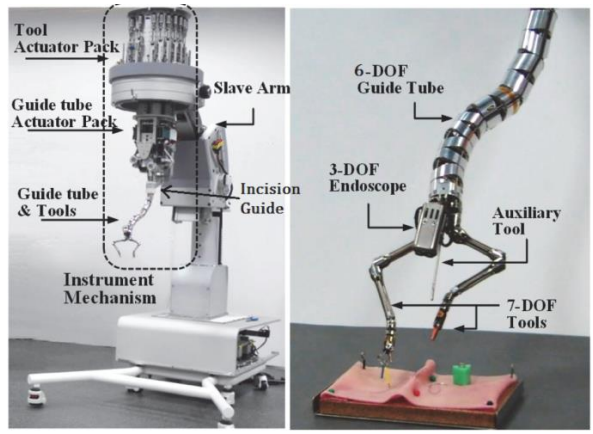


Fig. 1.5 SAIT single port access surgical robot; An active manipulation of guide tube, with 2 surgical instrument arms [11]

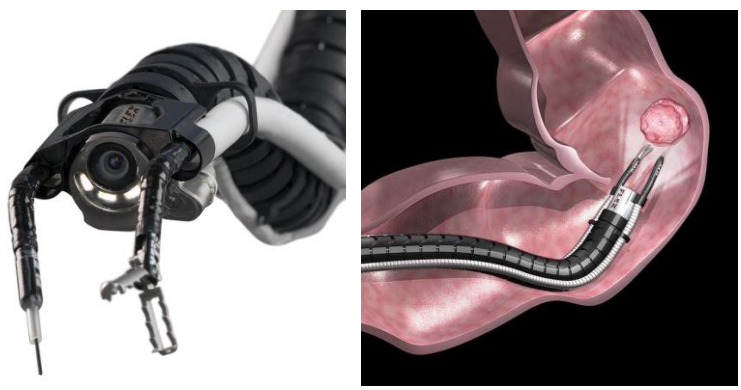

Fig. 1.6 Flex robotic Platform; 2 surgical instruments are guided by the central back-bone like structure [12]

## 1.2 Tendon-sheath mechanism

### 1.2.1 Application of TSM in flexible surgical instruments

A tendon-sheath mechanism (TSM) is widely used in commercialized endoscopic systems. It is comprised of a cable threaded in a hollow conduit, as shown in Fig 1.6. The cable or sometimes called wire rope acts as a tendon as it slides inside of the hollow conduit, acting as a sheath. There are many different concepts realizing a flexible endoscopic system, such as pneumatic actuation and using shape memory alloys, but one of the most common transmission modes is the TSM.

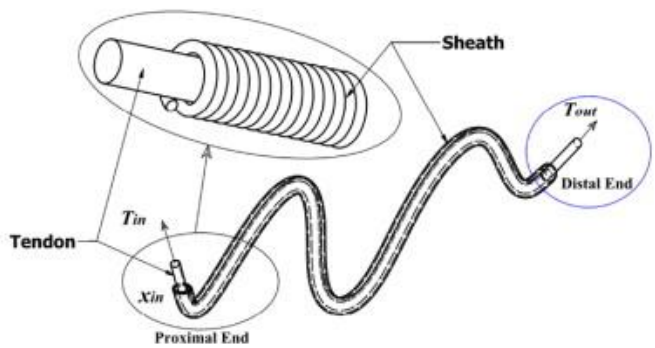


Fig 1.7 Schematic of Tendon-sheath Mechanism [13]

TSM is a key component in realizing flexible robotic instrument. When a tension is applied to the tendon to transfer the displacement driving the articulated joints at the distal end, naturally it will follow the shortest path. In conventional laparoscopic robotic instruments, the tendons are guided by a simple pulley-cable system as shown in Fig 1.6, and this is possible since the distance between the distal and the proximal end of the rigid tube will not change.

For flexible robotics instruments however, the distance between the distal and proximal end of the flexible tube will adapt to arbitrary path of the environment and the path will not be at the shortest distance possible. To follow an arbitrary path of

the flexible tube, a sheath serves as a passage guide for the tendons, enabling the transfer of motion in tortuous paths. For this reason, TSM has been used in many flexible surgical systems [14] [15] [16] [17]. A similar mechanism to TSM will be Bowden-cable mechanism and push-pull wire control.

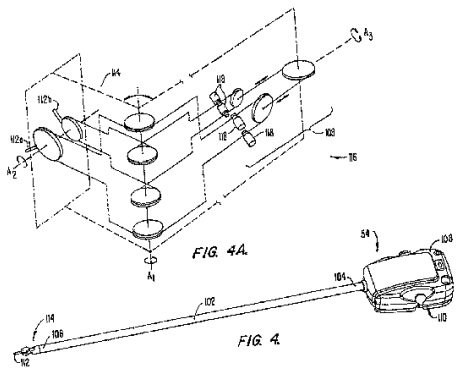


Fig. 1.8 Robotic surgical instrument of da Vinci system, driven by cable-pulley system [18]

For flexible robotics instruments however, the distance between the distal and proximal end of the flexible tube will adapt to arbitrary path of the environment and the path will not be at the shortest distance possible. To follow an arbitrary path of the flexible tube, a sheath serves as a passage guide for the tendons, enabling the transfer of motion under tortuous paths. A similar mechanism to TSM will be Bowden-cable mechanism and push-pull wire control.

### 1.2.2 Effects on motion transfer characteristics

Due to its many advantages of high maneuverability, lightweight, low cost, and simple design, TSM has enabled many researchers to realize flexible endoscopic systems. But a nonlinear phenomenon such as friction and backlash hysteresis present major challenges for motion control [19]. In TSM, this phenomenon arises from three different aspects: tendon elongation, friction and hysteresis, and the loss of motion.

Aside from the material properties of tendons, which will vary by the material of the selected tendon, the fact that flexible instruments are typically longer than conventional laparoscopic robotic instrument gives a disadvantage in total elongation of the tendon. In flexible surgical instruments, the total length must exceed the length of global positioning device (overtube, guide tube), and add extra length for translation motion. The total length of flexible instruments varies by systems but are generally in the range of 1500-2000mm whereas a typical laparoscopic instrument will not exceed 1200mm at most. Moreover, to resolve such issue, in case of laparoscopic instruments the tendon is reinforced with a hypotube to reduce the elongation as shown in Fig 1.8, in which case for TSM applied flexible instruments is not an option because the tendon has to run entirely through the sheath.


Fig. 1.9 Hypotube reinforced tendon in laparoscopic surgical instruments; tendon will be routed with a pulley to the driving element, at non-reinforced region

For tendons that are usually less than 0.5mm in diameter, the running length will be 3000-4000 fold or more relative to the diameter which amplifies the elongation effect. Means to reduce such elongation will be covered in detail in chapter 2.

Friction between the sliding tendon within the sheath also contributes to a nonlinear backlash hysteresis, which was confirmed by various studies [13] [20] [21]. Modeling such behavior has been studied in many literatures, which will be covered in chapter 1.3.

The loss of motion of sliding tendons within a sheath is another factor contributing to a backlash hysteresis as shown in Fig. 1.9. The clearance between the tendon and the sheath must be carefully designed to minimize such effect.

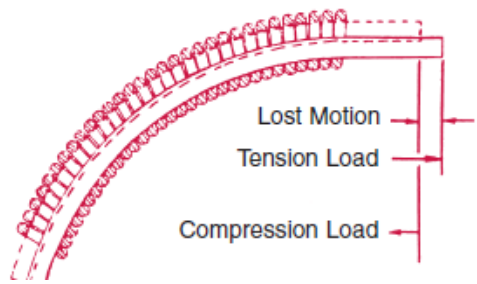


Fig. 1.10 Backlash and lost motion caused by tendon under tension within a sheath. [22]

## 1.3 Previous Studies

There have been several kinds of research that have addressed the nonlinear characteristics of tendon-sheath mechanism, many of which utilized analytical models of friction and motion. Although a work by Kaneko et al. [20] [21] did not provide any positional control scheme, the authors were able to describe the transmission of tendon tension in terms of static friction model with lumped mass model parameters. Palli et al. modeled the tendon-sheath mechanism with dynamic friction model along with the lumped mass model parameters [23] [24], which showed that when the motion of tendon-sheath mechanism is near zero velocity the discontinuity problem arises. Such study did not provide any control strategies to compensate for the errors. A set of partial differential equations to model the tendon segments across a tendon-sheath mechanism was proposed by Agrawal et al. [25] [26]. Due to its complexity of the governing equation, this approach was limited in fast calculations for real time application and moreover, the discontinuity problem near zero velocity was not resolved. Do et al. [19] proposed a method which utilizes a modified version of Bouc-Wen model of hysteresis. This approach successfully identified empirical parameters of customized Bouc-Wen model, but in the final step, a feedback loop from the output side of the TSM was included in the control scheme, which in most surgical robot applications is not a valid option. All the aforementioned studies have either assumed that the shape variation of TSM did not severely affect the hysteretic output and oversimplified the shape variation effects or did not consider shape variation as an issue for modeling. For instance, in the study by Do et al. [19], the output was assumed to only depend on the accumulated curve angles from the input side to the output side. In some studies such as [23] [24] [26] the TSM was wound in 180 degrees, which considering the actual application where the flexible surgical instruments will be of use, is a rare and unrealistic situation. Also, in some studies the model parameters had to be distinct for different input types

which ultimately limits the possibility to be applied in real situations where the input will be delivered ambiguously through the master controller by the operator (i.e., Surgeon). Hence to overcome these shortcomings, a hysteresis model that captures the intraoperative shape variation of the TSM and adequate inversion algorithm to compensate for the hysteresis in real-time is desired.

## 1.4 Research objectives

The main objective of this research is to derive a model capturing a nonlinear backlash hysteresis of TSM in flexible surgical instruments and develop a control scheme for a precise position control. This research can be categorized into four major topics.

The first topic is to configure a tendon-sheath mechanism with a reasonable amount of consideration of the actual surgical environment in practice, and some regulatory issues, being a medical device application. Of course, the configuration, especially the size (diameter) of the tendon and sheath will vary by case to case, according to the specific size constraints that is applicable for different flexible surgical platforms. Such size constraints of this study will be set as following: flexible surgical instruments of 6mm outer diameter applicable to 19mm overtube. The configuration of the tendon-sheath mechanism will greatly affect the nonlinear backlash hysteresis characteristics and hence the reasoning of selection and fabrication methods of TSM components will be described.

The next topic is observing the backlash hysteresis behavior and exploring how the shape of the TSM affects the outcome in motion control perspective. An experiment setup was designed to accomplish this observation, and TSM is tested under various combinations of shape configurations, given various types of input signals.

The third topic is to model the observed hysteresis. As described in the previous section, since it is infeasible to obtain any feedback at the tool tip of the flexible instrument, open loop feedforward and computationally low cost inversion model that captures the varying shape configuration of the TSM is crucial in achieving precise motion control.

The last topic is an actual application to the articulated manipulator. A single-segment antagonistic, redundant joint manipulator driven with four tendons, is

designed, and its kinematics was solved. The proposed model is applied to each tendon and with an optical tracking device, the positional and orientational accuracy of the manipulator is assessed.

# Chapter 2. Configuration and fabrication of TSM

In this chapter, configuring a tendon-sheath mechanism for the implementation of a previously developed 6mm outer diameter flexible surgical instruments (Fig. 2.1) with 19mm over tube (Fig. 2.2) will be described. For driving the double-segment articulated joints, there must be four tendons for each of the distal and proximal segment and two for end effector (i.e., forceps) control, amounting to total of ten tendons. Also, two electric cables must fit internally for operating an electro-cauterization device. To prevent tangling of all 12 elements inside the flexible tube, a multi-lumen with ten channels is fitted inside the tube, as shown in Fig.2.4. As such, the size constraints of the components for previously developed system is determined considering the available clearance between the relative components that are assembled together, feasibility in assembly and machining capabilities. The size constraints of each components are organized in Table. 2.1.

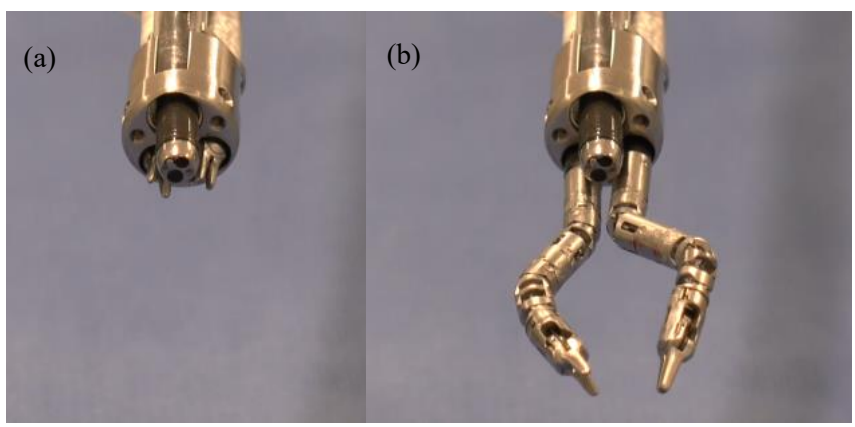


Fig. 2.1 Two flexible surgical instruments and an endoscopic camera inserted in to an overtube: (a)idle position, (b) triangulated pose for local manipulation

Fig. 2.2 Steerable five-channel overtube with outer diameter 19mm

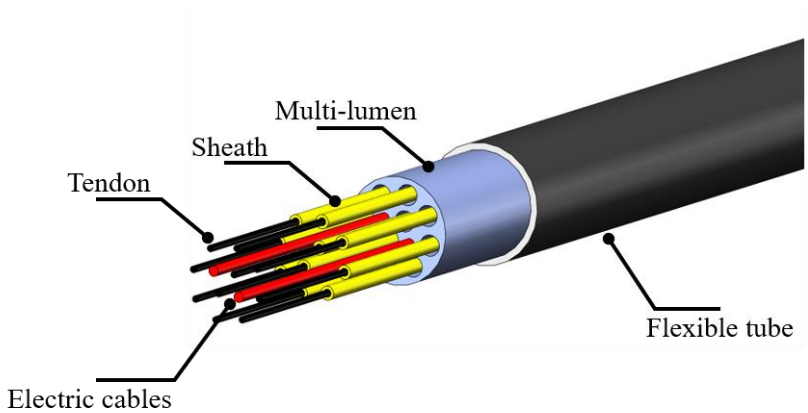


Fig. 2.3 Components inside a flexible surgical instrument

The description of the sheath used in this research will be next, followed by the description of tendons and its treatments. The fabrication of fittings will be the final item of this section.

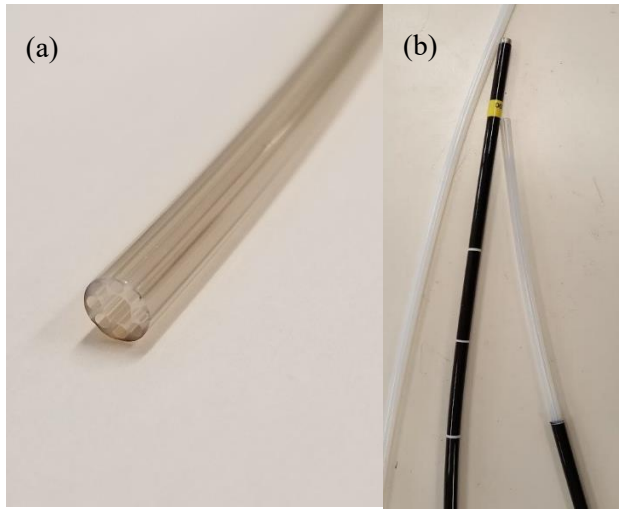


Fig. 2.4 (a)PTFE Multilumen, (b)Multilumen inserted in flexible tube

Table 2.1 Constraints of the previously developed system.

| **Constraints** | **Overtube** | **Flexible tube** | **Multilumen** | **Sheath** | **Tendon** |
|---|---|---|---|---|---|
| Outer Diameter | 19mm | 6mm | 4.5mm | ≤0.85mm | ≤0.40mm |
| Inner Diameter | - | 4.8mm | 1mm (Lumen) | ≤0.45mm | - |
| Length | 700mm | 1200mm | 1200mm | 1100mm | 1400mm |
| Minimum bend radius | 35mm | 35mm | 35mm | 35mm | 35mm |
| Maximum Angle | 90° | 90° | 90° | 90° | 90° |
| Break load | - | - | - | - | ≥200N |

## 2.1 Sheath

Selecting a proper sheath is critical in configuring a TSM. Sheath is often called wire coils or coil pipes, which is a hollow coiled wire that is flexible and capable of withstanding compression. Fig. 2.5 shows three different types of wire coils that are commercially available.

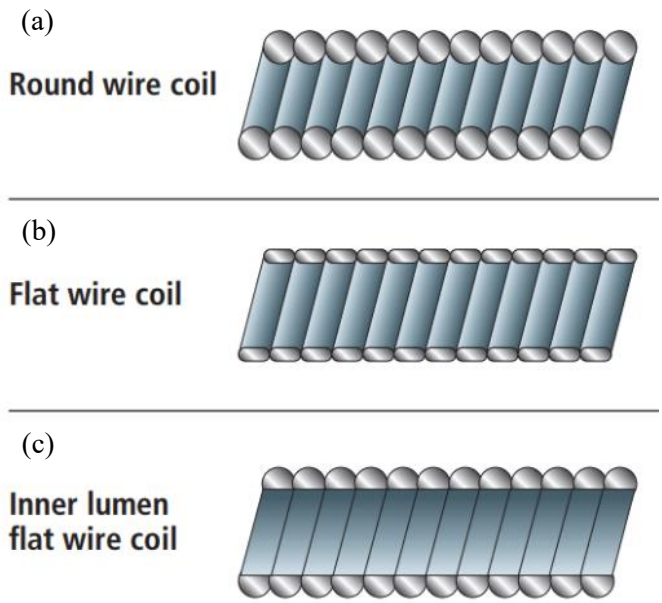


Fig. 2.5 Cross section of different types of coil wires: (a) Round wire coil, (b) Flat wire coil (c)Inner lumen flat wire coil [27]

Among the different types of wire coils, the inner lumen flat wire coil is invalid for application, given the minimum outer diameter achievable was 2mm, which is far greater than the size constraint of less than 0.85mm. The difference between the round wire coil and flat wire coil is the wire's cross-sectional shape. While round coil has a price advantage compared to flat wire coil, flat wire coil has greater compression resistance due to its shape. The round wire coil when under compression caused by the tension of the tendons inside, the coil will collapse on to

each other resulting in a deformed and shortened coil. For this reason, a flat wire coil was used with 0.460mm inner diameter, 0.800mm outer diameter, as shown in Fig. 2.6. (Part No.185026, Endoscopic Development Company, USA).

Fig. 2.6 Close up image of EDC flat wire coil.

## 2.2 Configuration of Tendon

### 2.2.1. Cable

As described in the introduction section, to minimize the nonlinear hysteresis phenomena, the elongation of the tendon must be minimized. There are two factors that affect the elongation properties of the cable.

The first arises from the material of cable which is called an elastic stretch. Across the studies regarding the development of flexible surgical instruments, due to its availability and low cost, stainless steel cables (SS316 or SS304) are widely used. In the commercial medical robotics field however, due to safety concerns and regulatory issues, commercialized robotic laparoscopic instruments commonly use tungsten cables which can provide greater margin of safety, longer product life and less elongation. To prove the commercial applicability in this study, TSM is configured with tungsten cables.

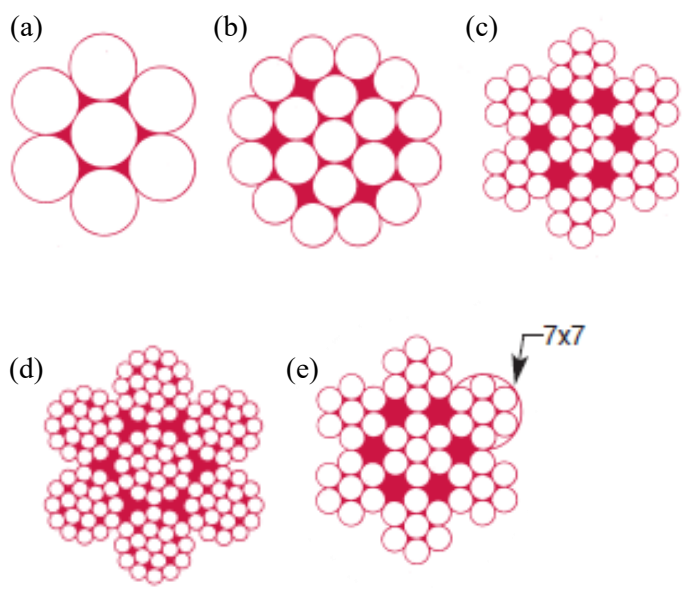


Fig. 2.7 Cross section of common construction of cables: (a) 1x7, (b) 1x19, (c) 7x7 (d) 7x19 (e)7x7x7 [28]

The second, constructional elongation, arises from the stranding of a cable. When the cable is in tension the space between the strands becomes tighter, which consequently contributes to total elongation of the cable. This is typically reported to be less than 2% at breakload, in which case for TSM using 1200mm of cable and delivering motion control in the range of 10-12mm this is a factor that cannot be ignored. Constructional elongation can be reduced by proof loading, which prestresses the cable to remove the constructional stretch. Proof loading is generally done at 60% of the rated breaking strength. Also, this can be mitigated by preloading the cables in all the operating range when in use. Additional treatment such as radially swaging the cable further reduces the constructional stretch. Fig. 2.7 shows common constructions for a cable. When selecting a construction under the same outer diameter, the break load, minimum bend radius and flexibility must be considered. Table 2.2 summarizes the characteristics of each construction for exemplary outer diameter of 1.0mm.

Table 2.2 Characteristics of different constructions for 1mm OD cable [29]

| **Construction** | **Wire diameter [mm]** | **Total number of wires** | **Breaking load [N]** | **Flexibility** | **Minimum bend radius [mm]** |
|---|---|---|---|---|---|
| 1x7 | 0.35 | 7 | 1127 | Low | 53 |
| 1x19 | 0.20 | 19 | 1078 | | 30 |
| 7x7 | 0.11 | 49 | 784 | | 17 |
| 7x19 | 0.07 | 133 | 833 | | 11 |
| 7x7x7 | 0.04 | 343 | 715 | High | 6 |

Considering all the factors above, a 7x19 tungsten cable with 0.381mm outer diameter was custom manufactured. (Fort Wayne Metals, USA) The final outer diameter of 0.381mm was achieved by radially swaging a 0.419mm cable. To reduce the constructional stretch, radial swaging and proof loading was applied, and black oxide coating for smooth operation and corrosion resistance was also added. Fig 2.8 shows the tungsten tendon fitted inside the sheath, and Table 2.3 summarizes the detailed specifications of the produced tendon

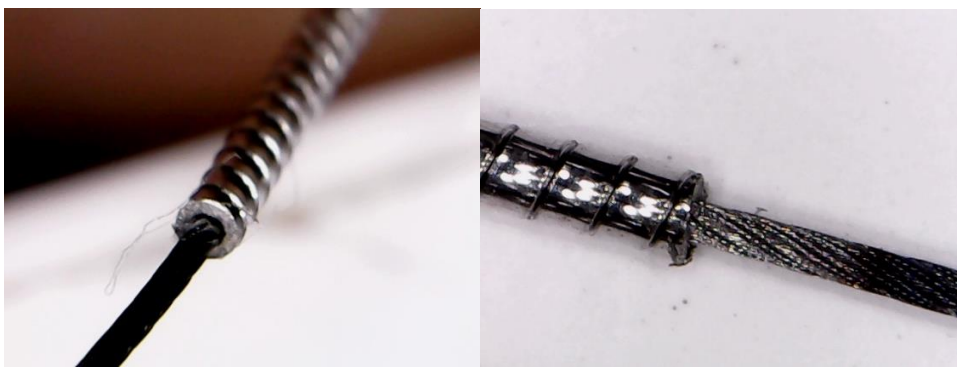

Fig 2.8 Tungsten tendon fitted inside the sheath

Table 2.3 Specifications of the custom manufactured tungsten tendon

| **Properties** | **Specification** |
|---|---|
| Material | Tungsten |
| Construction | 7x19 |
| Wire diameter | 0.028mm |
| Finished diameter | 0.381mm |
| Breakload | 235N |
| Elongation at breakload | 0.3% |
| Treatments | Black oxide coating, Radial swaging, Proof loading at 60% breakload, Electrofused |

### 2.2.2. Fitting

A final issue in implementing a working TSM is applying a fitting to the tendon. This is often called a stop sleeve, and it is forged at the end of the tendon to serve as a force acting point. The envelope pocket dimension for the stop sleeve to be applied at the distal end of the articulated joint is 0.9mm square with 1.5mm in length. Also the requirement was that the stop sleeve should attain minimum of 80% of breakload of the tendon. Since this is a highly custom application, a swaging die was designed as shown in Fig. 2.9 and installed as shown in Fig. 2.11.

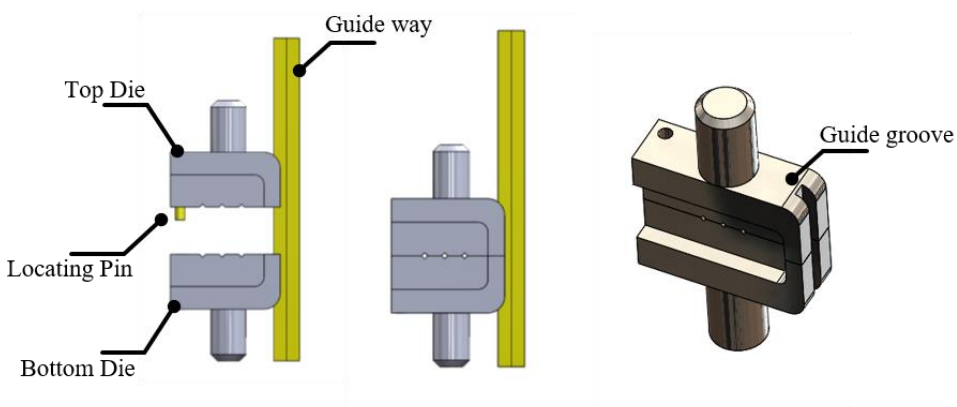


Fig. 2.9 Design of swaging die guided with a guide groove and locating pin

The swaging die is machined of SCM45, and was fitted to a pneumatic press (HP-1000, Hyundae Machinery & Electric Co., Korea) as shown in Fig.2.10. The specification of the pneumatic press is organized in Table. 2.4.

Table 2.4 Specifications of HP-1000 pneumatic press

| **Specification** | |
|---|---|
| Tonnage capacity | 1 ton |
| Ram Stroke | 100mm |
| Daylight | 250mm |
| Bolster size | 300mm x 260mm |
| Pneumatic cylinder inner diameter | 180mm |
| Reach | 140mm |

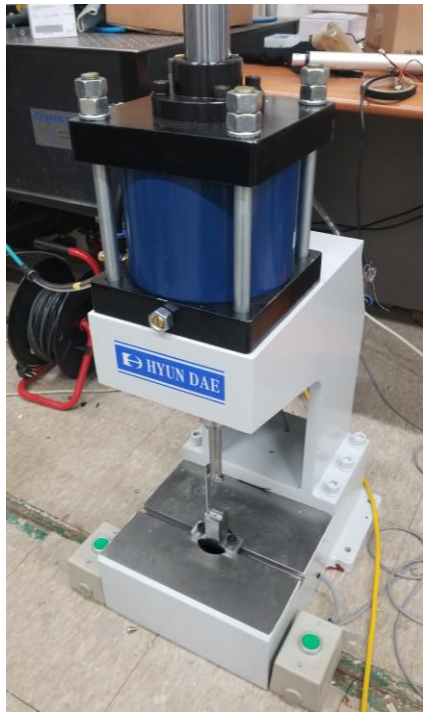


Fig. 2.10 Pneumatic press HP-1000

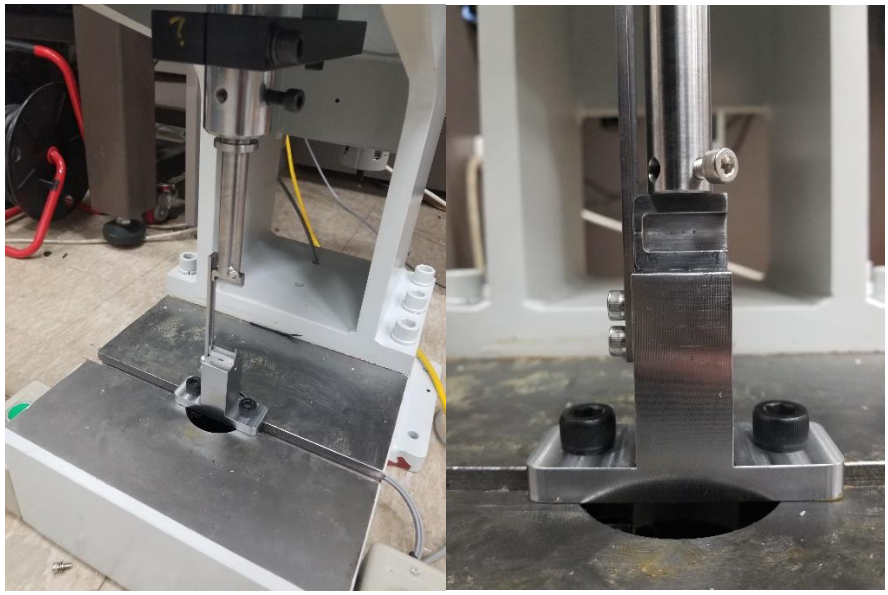

Fig. 2.11 Swaging die installed to a pneumatic press

The ferrule used for swaging has a dimension of 0.820mm outer diameter, 0.410 inner diameter and 1.2mm long. The snapshots of ferrules before and after swaging is shown in Fig. 2.12.

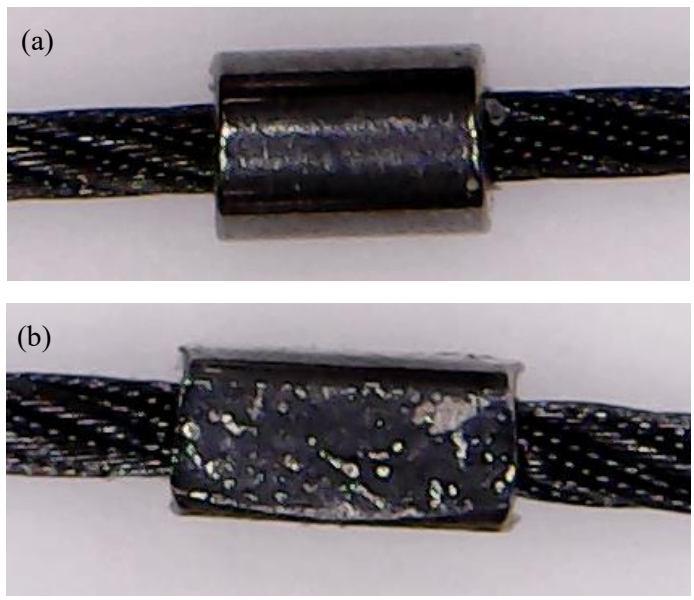


Fig. 2.12 Swage ferrule: (a)before and (b) after swaging

The finished dimension was microscopically measured to be 0.747mm cuboid with 1.3mm length. (Fig. 2.13) Three trials of breakload testing revealed an average of 198N of breakload which was 84.2% of the tendon breakload, and applicable for use.

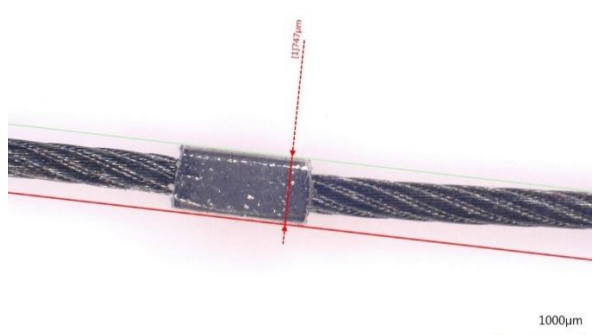


Fig. 2.14 Microscopic measurement of swaged ferrule

# Chapter 3. Hysteretic behavior of TSM

## 3.1. Experiment setup

### 3.1.1 Experiment design

To identify how the output characteristics change in different shape configurations, a set of experiments is designed and will be presented in this section. As described in chapter 1, an overtube is a global positioning device that will serve as a fixture for the local manipulation of flexible surgical instruments. If the instruments are translated far out of the overtube, it will be unable to be fixed in place to perform any local manipulation due to its flexibility. Hence, it is safe to say that the flexible surgical instruments will attain the same shape of that of an overtube while in use.

In this study, parameters characterizing the shape of a flexible instruments are the curve angle and radius of curvature which will be denoted $\phi$ and $r$, respectively. The values of each $\phi$ and $r$ to be tested are organized in Table 3.1.

Table3.1 $\phi$ and $r$ shape parameters for experiment

| **Curve angle ($\phi$)** | **Radius of curvature ($r$)** |
|---|---|
| 15° | |
| 30° | 30mm |
| 45° | 45mm |
| 60° | 60mm |
| 75° | 75mm |
| 90° | |

For every curve angle, different radius of curvature is tested, producing 24 different sets of experiments. Three types of input signal excitation were given to each set, amounting to 72 data sets. The input signals are shown in Fig.3.1.

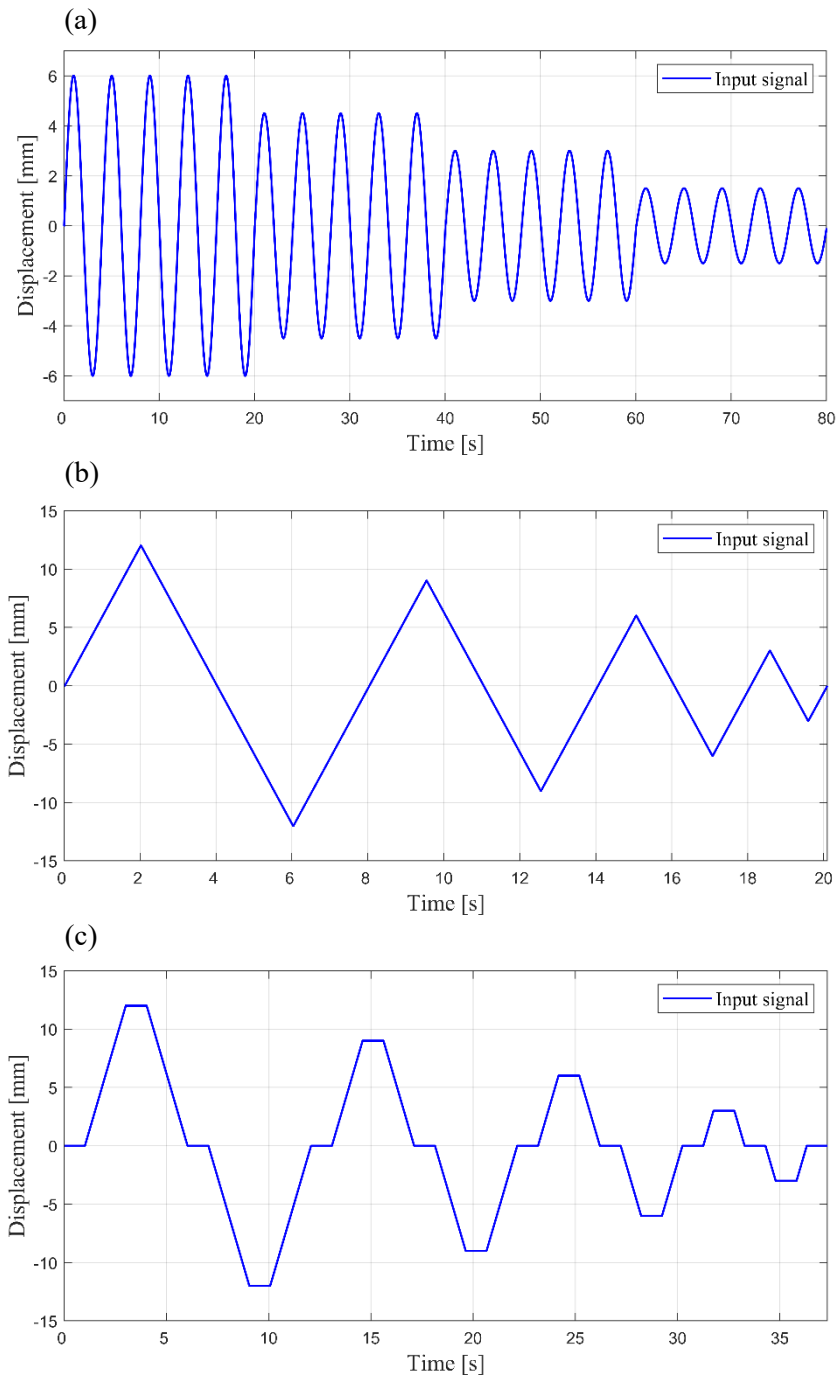


Fig.3.1 Three different input excitations for experiments: (a) sinusoidal with decreasing amplitude, (b) triangular with decreasing amplitude (c) trapezoidal with decreasing amplitude

### 3.1.2 Hardware design

In this section, hardware design for the experiments described in previous section will be presented. An input and a follower module are shown in Fig. 3.2.

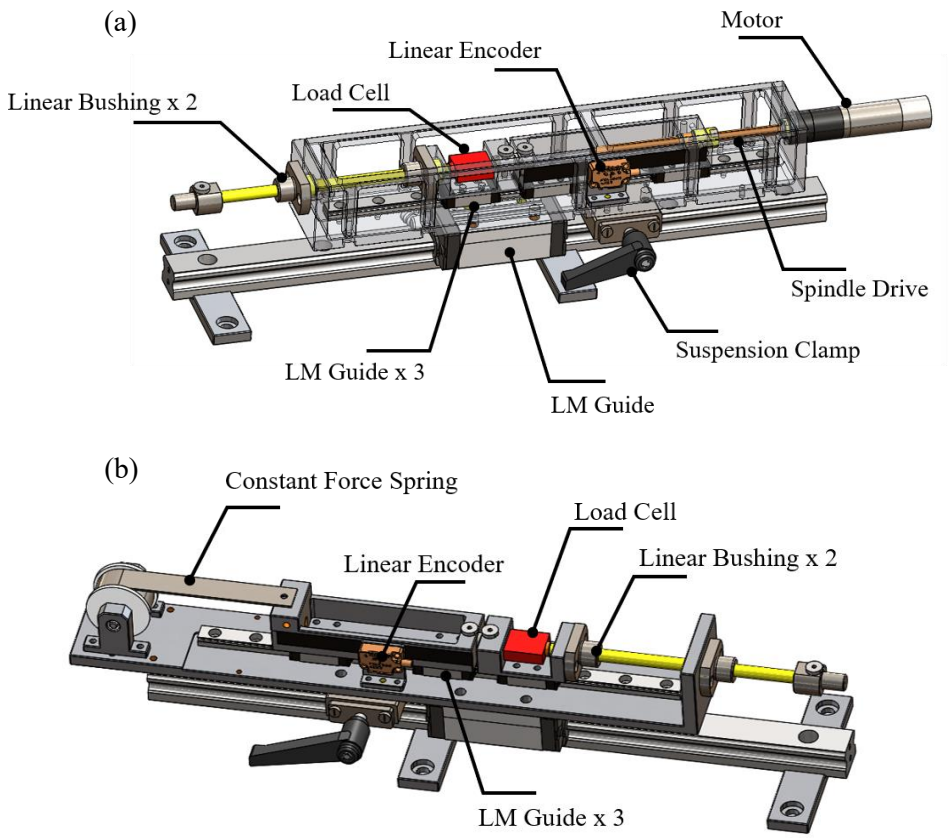


Fig. 3.2 Hardware design of experiment setup: (a)input module, (b)follower module

The input module is driven by a spindle drive BLDC motor (EC-Max 16, Maxon Motor, Switzerland). Position of each the input and the follower module are measured via an optical linear encoder (ATOM2T-100, Renishaw, UK) that is installed to the side of the moving body. Loadcell (SBAT-02, CAS, Korea) is installed in both modules to monitor the tension in both sides. The follower module is installed with a constant force spring to emulate the pretension while the TSM is

under operation. All the force bearing components are machined with SS304 alloy while the structural components are machined with AL6061 alloy. The sheath is suspended at both sides with a sheath suspension bracket as shown in Fig. 3.3.

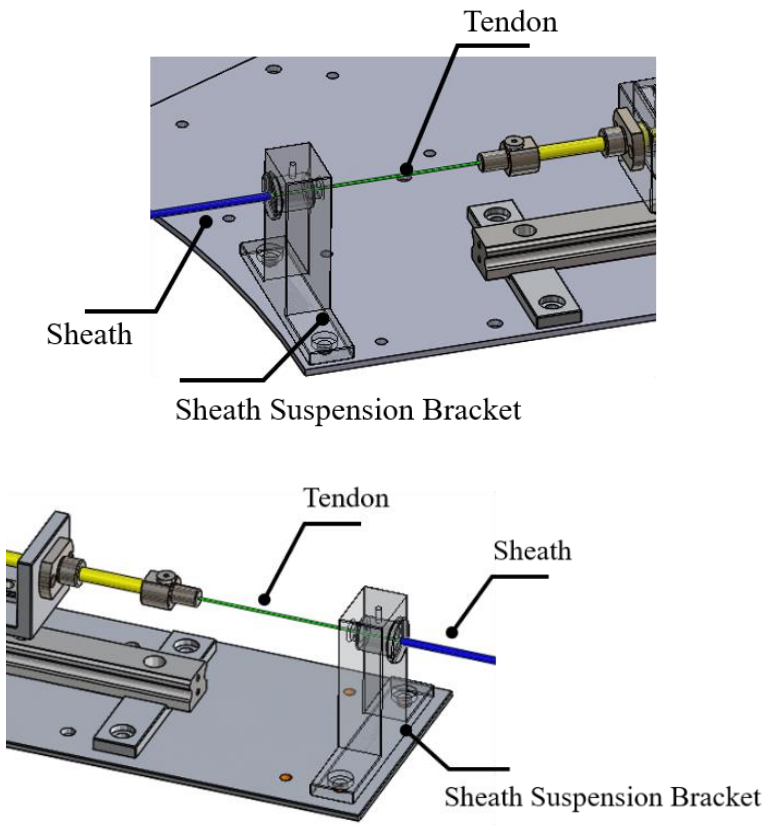


Fig 3.3 Sheath suspended at both sides: (a) at input module, (b)at follower module

To change the curve angle of the TSM, while the follower module is stationary, the input module's angular position is manually changed by installing to the respective position at the curve angle guide plate, which is tapped and drilled at each angular location as shown in Fig. 3.4 and Fig. 3.5. The overall setup is shown in Fig. 3.6. A curvature guide was designed and machined with ABS polymer as shown in Fig. 3.6 and changing the curvature guide for each experiment is illustrated in Fig. 3.7.

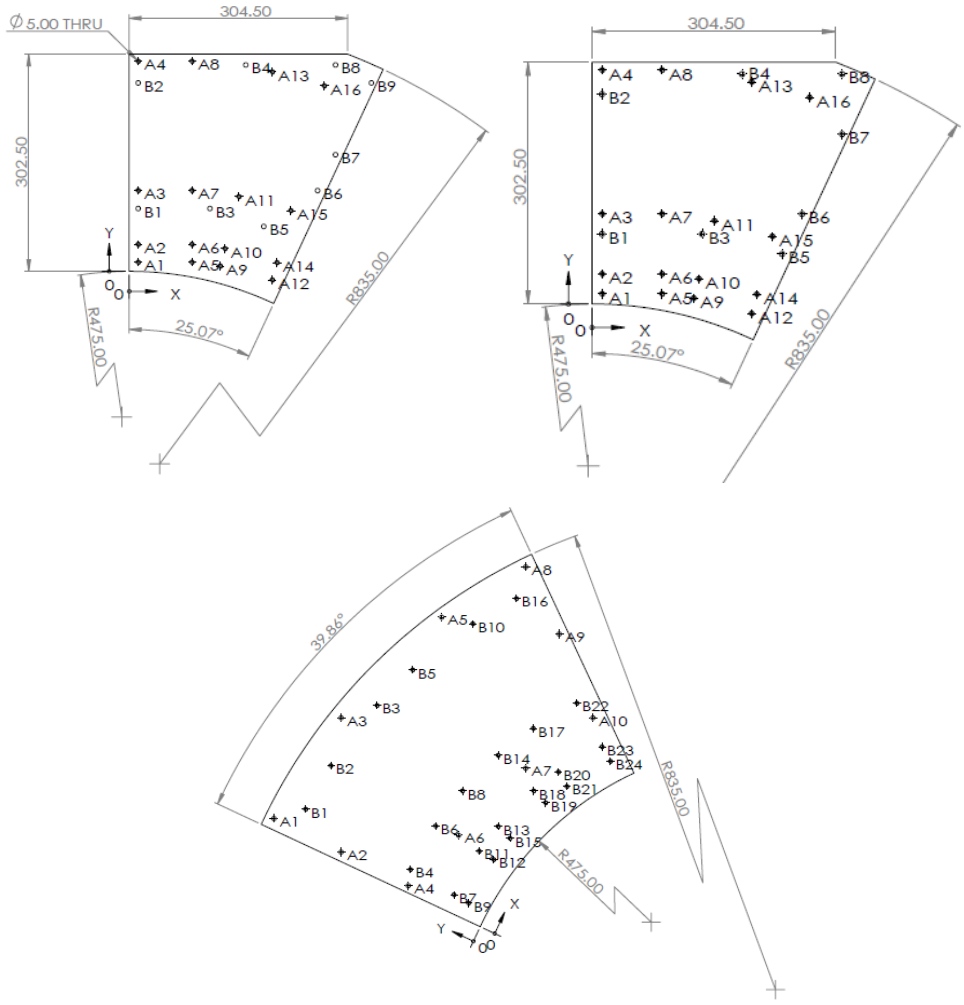


Fig. 3.4 Curve angle guide plates: (a) 75° - 95° ,(b) 0° - 15° ,(c) 30° - 60°

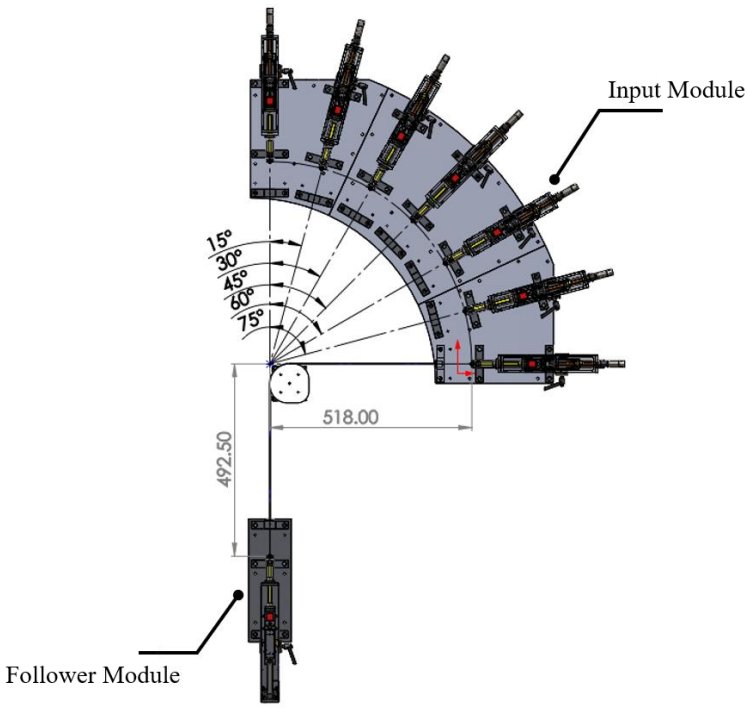


Fig. 3.5 Changing the curve angle of TSM, shown in 90°

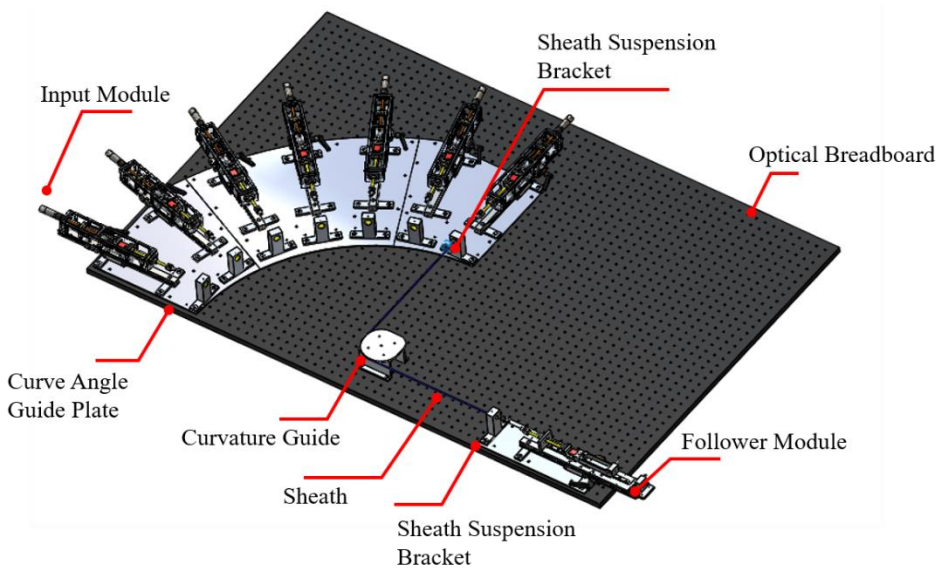


Fig. 3.6 Experiment hardware setup

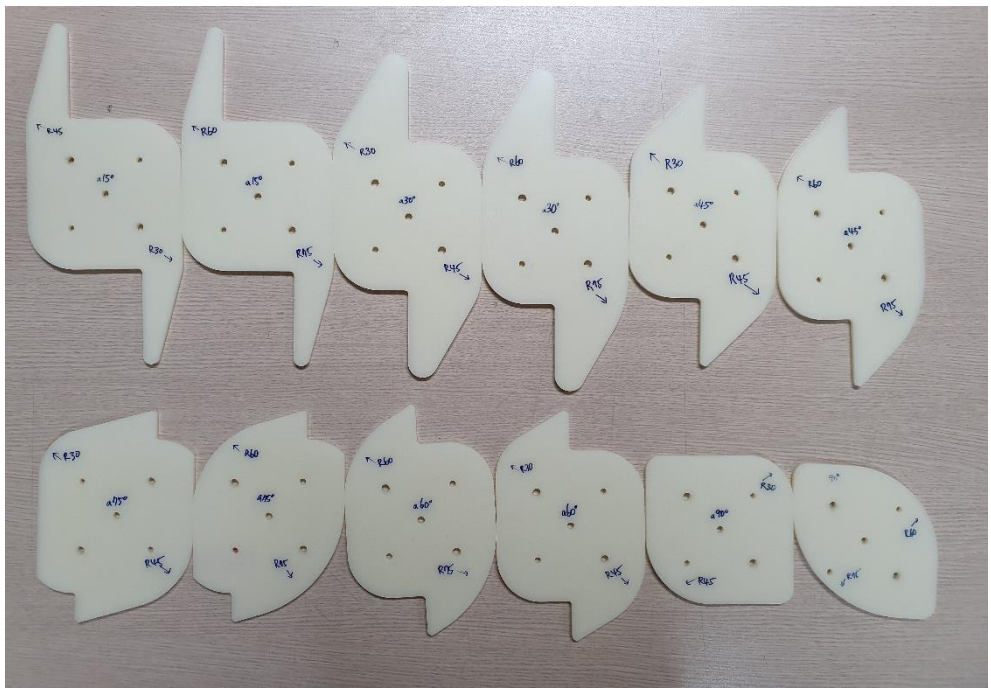

Fig. 3.7 Machined curvature guides for every curve angle

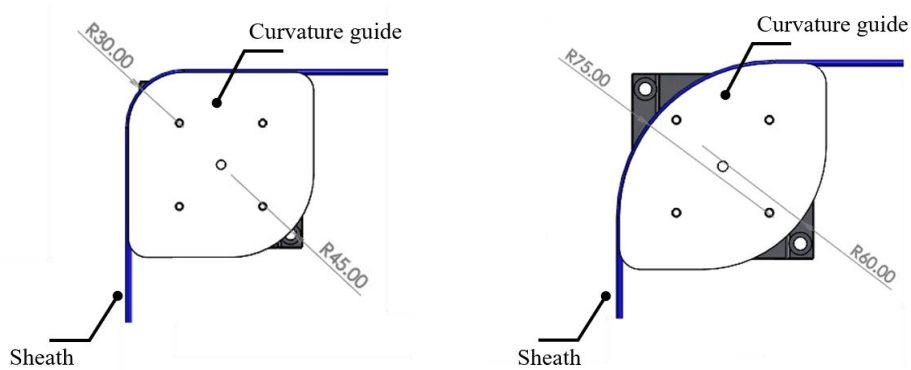


Fig. 3.8 Curvature guides for different radius of curvature: (a)r=30mm (b)r=75mm for 90° curve angle.

For motor servo control, a BLDC motor driver (EPOS2 24/5, Maxon Motor, Switzerland) is used. A National Instrument cRIO-9082 real time system with Xilinx FPGA is used for data acquisition of the load cell and linear encoder and controlling

the servo motor. CAN (Controller Area Network) protocol was used to transfer signal between NI9082 and EPOS2 with the use of high-speed CAN module NI-9853. NI Labview was used to configure real time control loop of 10ms for the BLDC motor and for compiling data acquisition FPGA logic. Fig. 3.8 shows the complete assembly of electric and mechanical components.

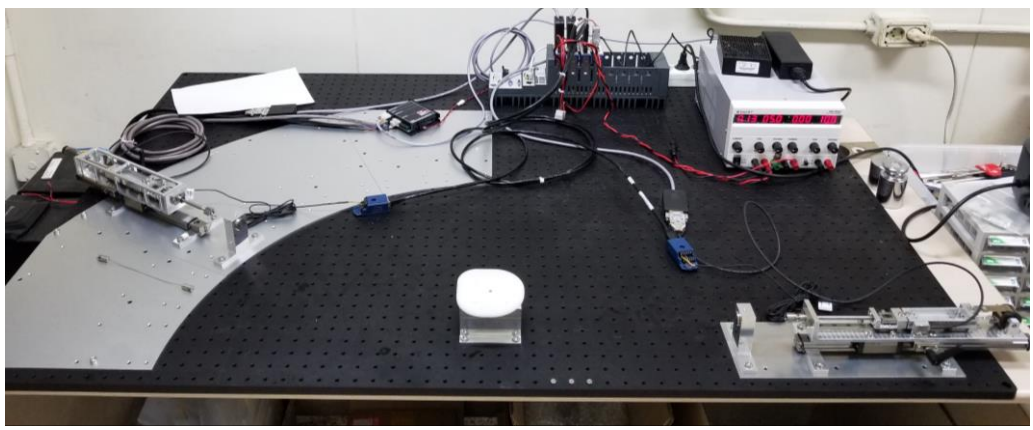

Fig. 3.9 Complete assembly of electric and mechanical components

## 3.2. Experiment results

### 3.2.1. Effect of curve angle variation

In this section, the result of changing the curve angle while the radius is maintained, will be presented. The input and output displacement are normalized by the maximum amplitude of input. The outputs at different curve angles along with the input signal are plotted, and the input-output map that shows the hysteresis curve are presented for each curve angles. The result will be summarized in chapter 3.2.3.

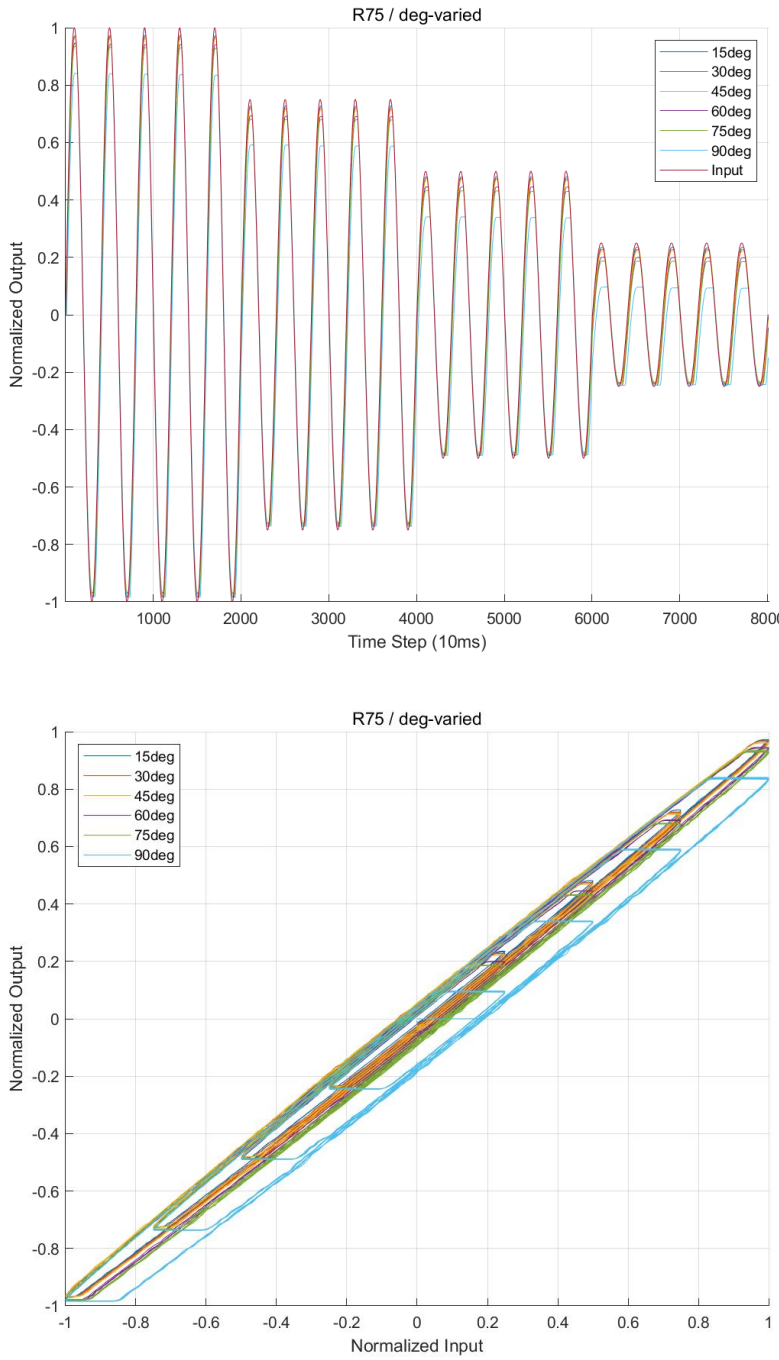


Fig. 3.10 Experiment results for R=75mm: (a)Output and input measurements for different curve angles, (b) Input-output map for different curve angles

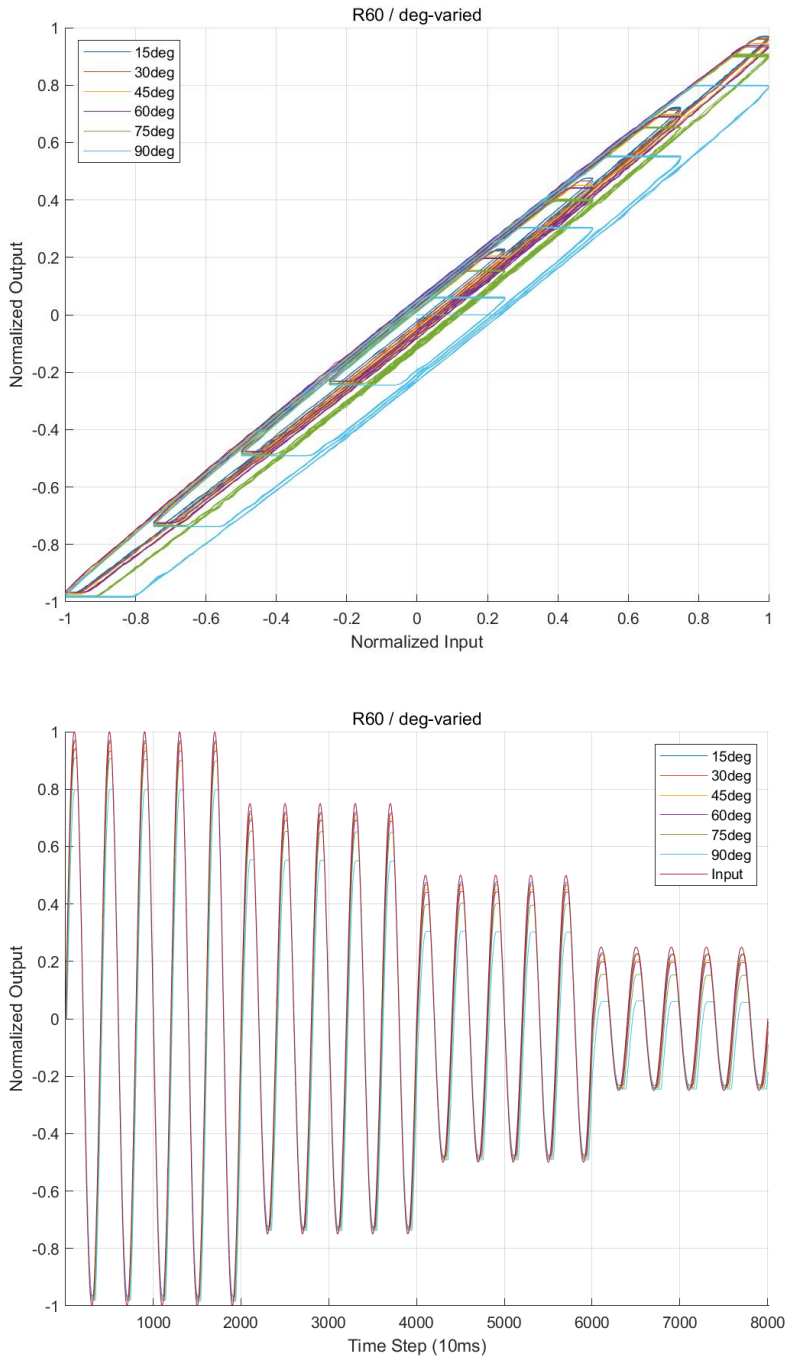


Fig. 3.11 Experiment results for R=60mm: (a)Output and input measurements for different curve angles, (b) Input-output map for different curve angles

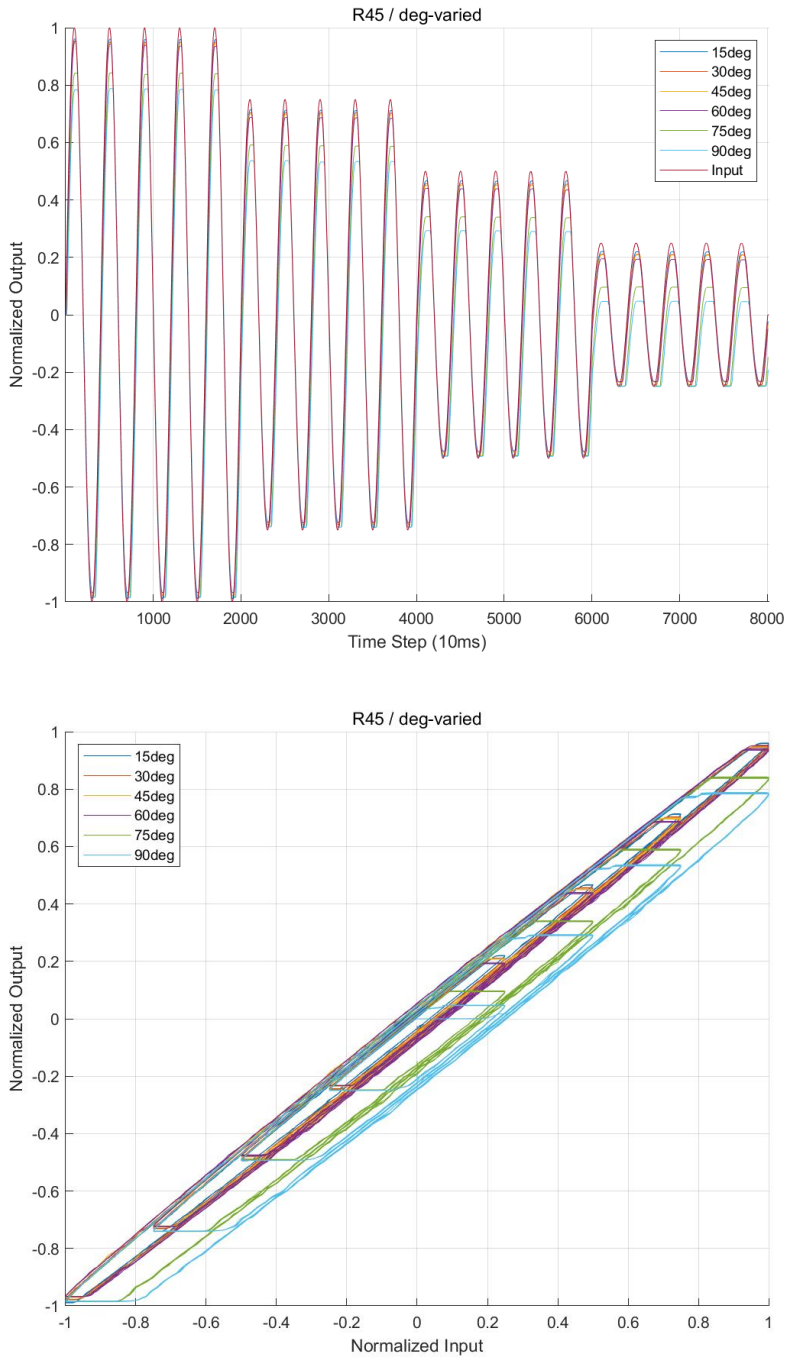


Fig. 3.12 Experiment results for R=45mm: (a)Output and input measurements for different curve angles, (b) Input-output map for different curve angles

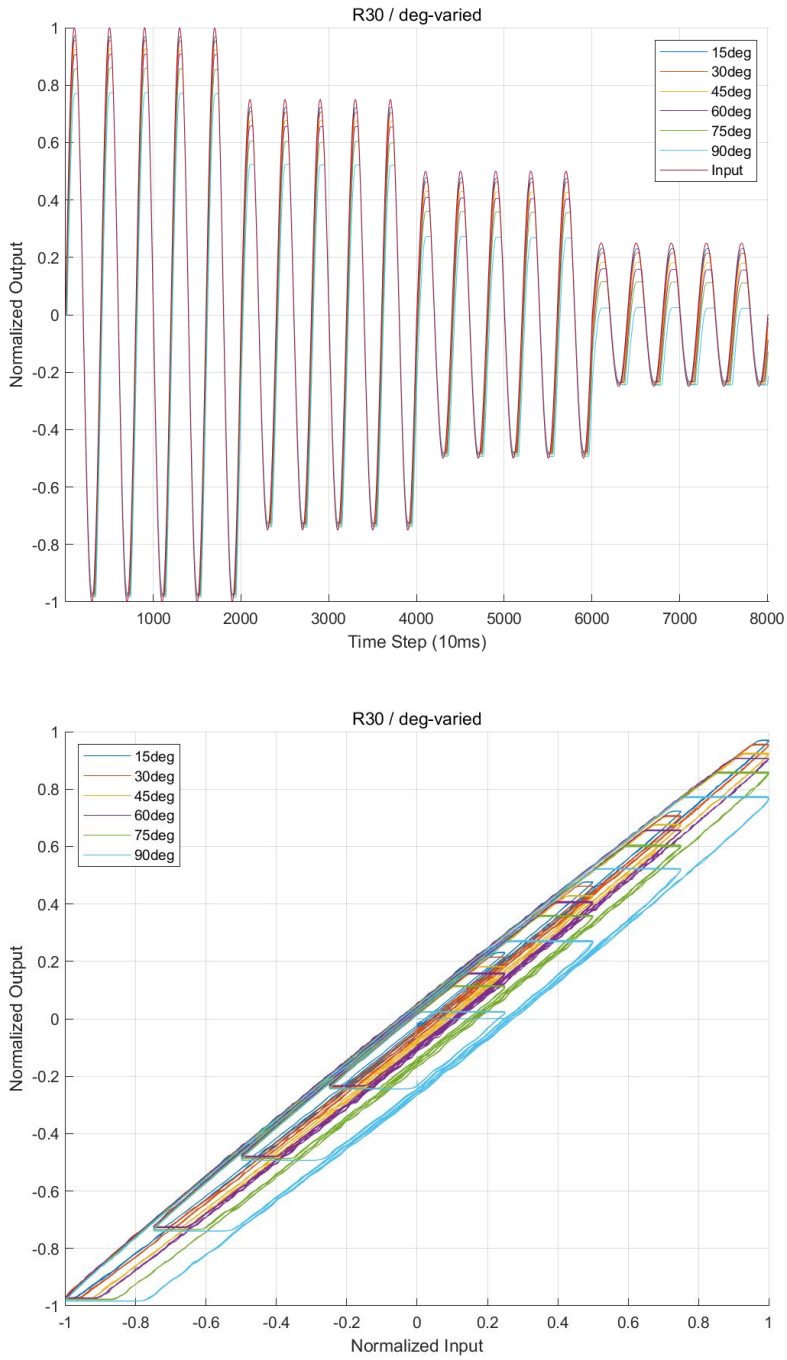


Fig. 3.13 Experiment results for R=30mm: (a)Output and input measurements for different curve angles, (b) Input-output map for different curve angles

### 3.2.2. Effect of radius of curvature variation

As opposed to the previous section, the result of varying the radius of curvature is while the curve angle is maintained, will be presented in this section. The input and output displacement are normalized by the maximum amplitude of input. The outputs at different radii along with the input signal are plotted, and the input-output map that shows the hysteresis curve are presented for each radius. The result will be summarized in chapter 3.2.3.

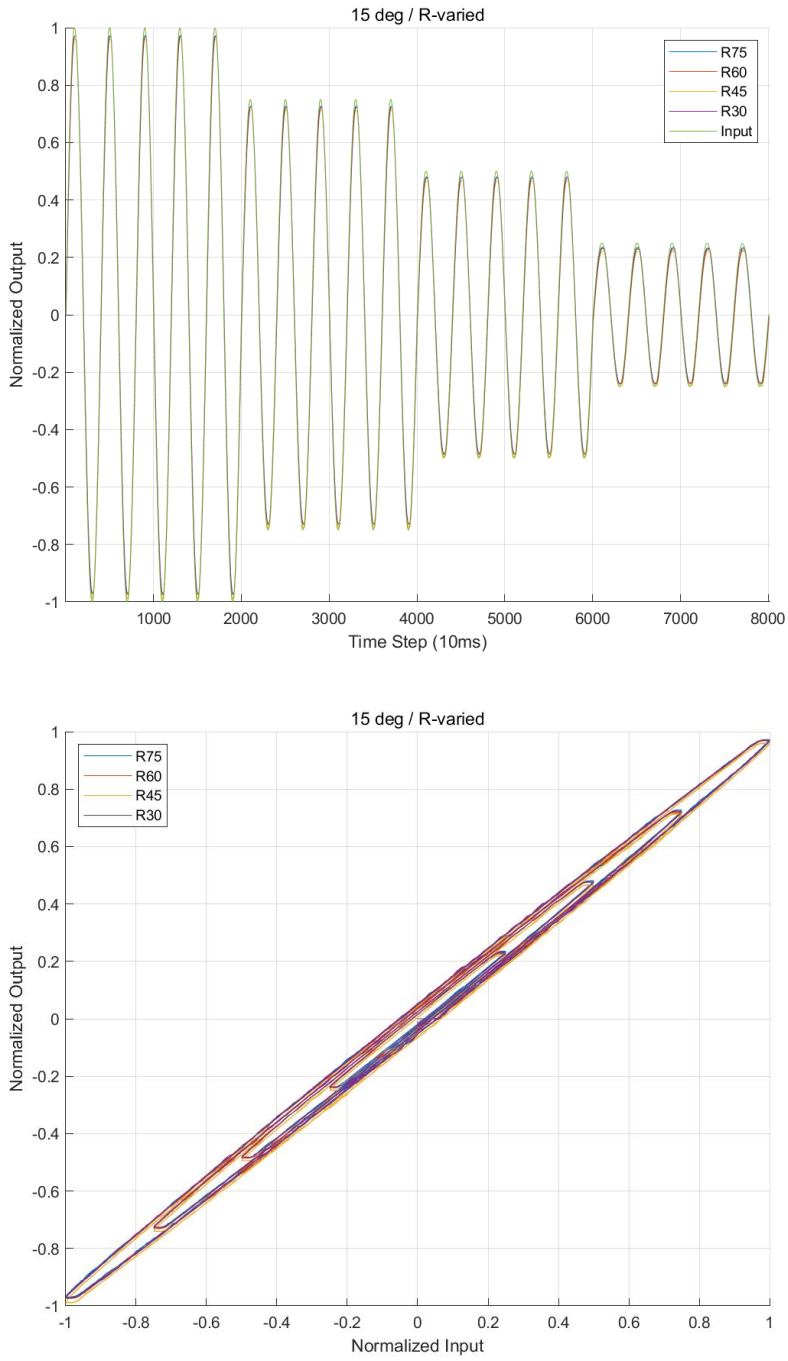


Fig. 3.14 Experiment results for $\phi = 15^{\circ}$ : (a)Output and input measurements for different curve angles, (b) Input-output map for different curve angles

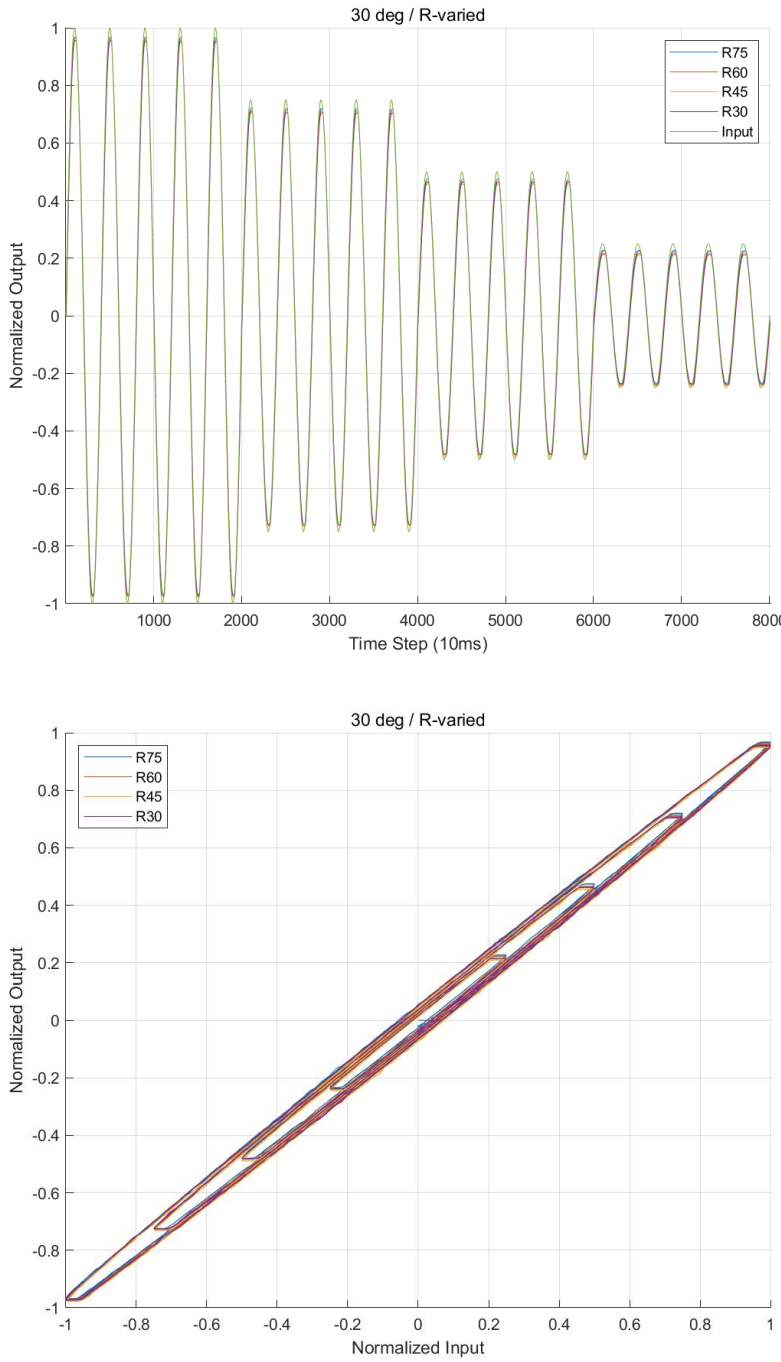


Fig. 3.15 Experiment results for $\phi = 30^{\circ}$ : (a)Output and input measurements for different curve angles, (b) Input-output map for different curve angles

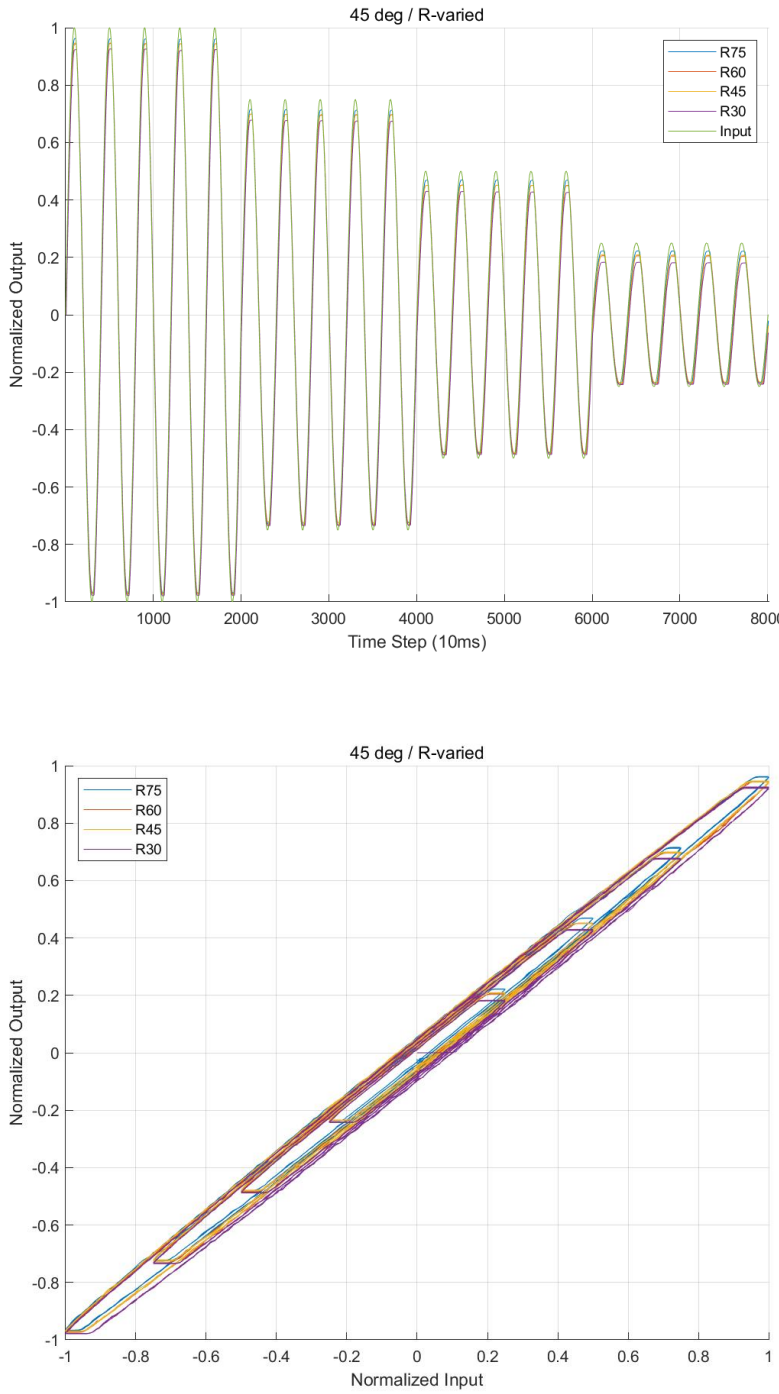


Fig. 3.16 Experiment results for $\phi = 45^{\circ}$ : (a)Output and input measurements for different curve angles, (b) Input-output map for different curve angles

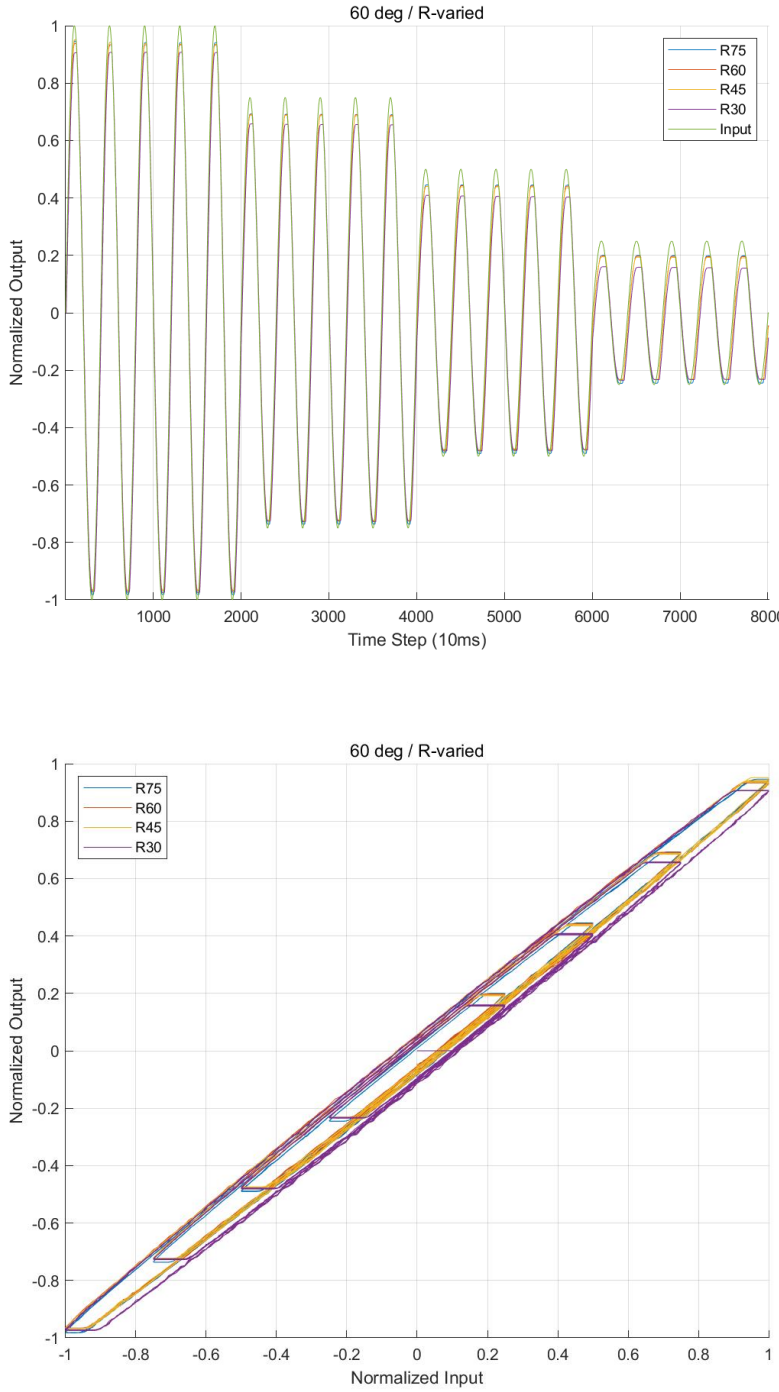


Fig. 3.17 Experiment results for $\phi = 60^{\circ}$ : (a)Output and input measurements for different curve angles, (b) Input-output map for different curve angles

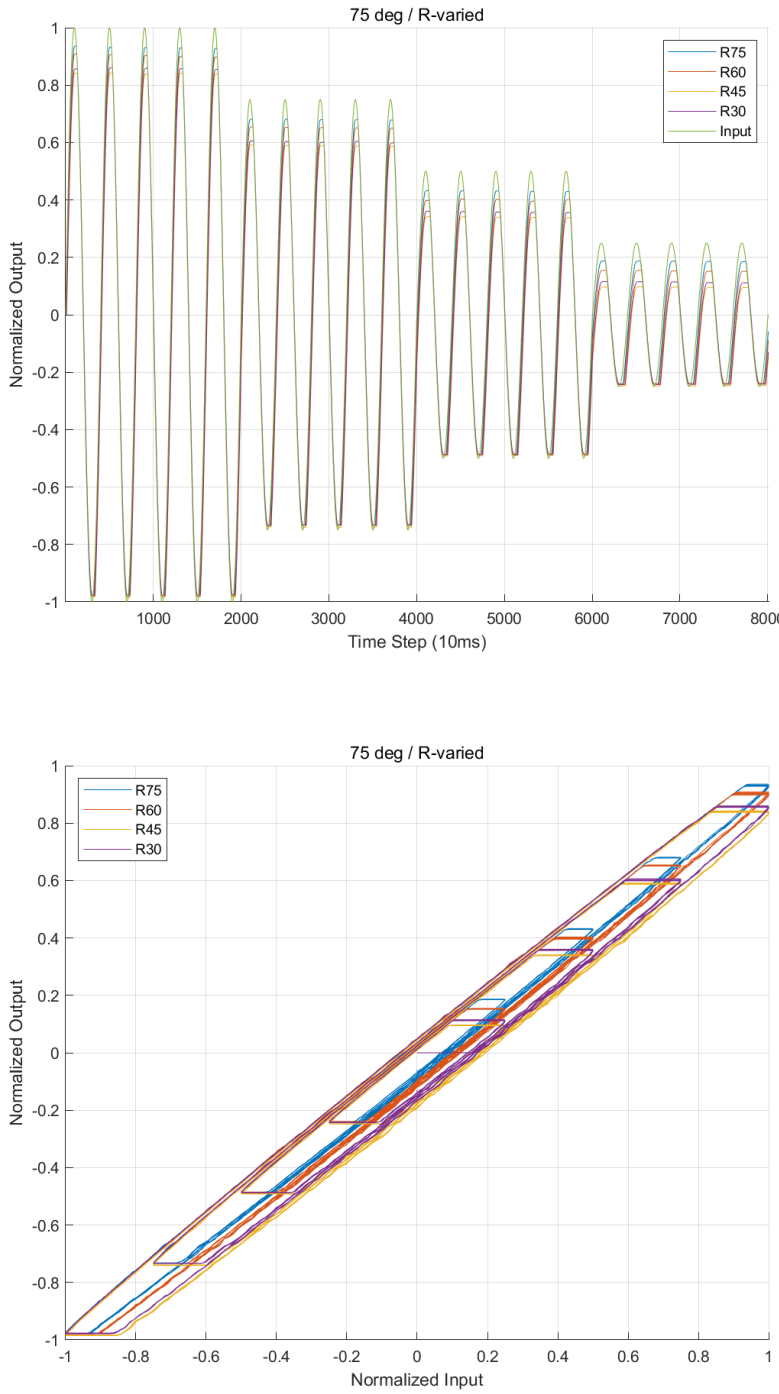


Fig. 3.18 Experiment results for $\phi = 75^{\circ}$ : (a)Output and input measurements for different curve angles, (b) Input-output map for different curve angles

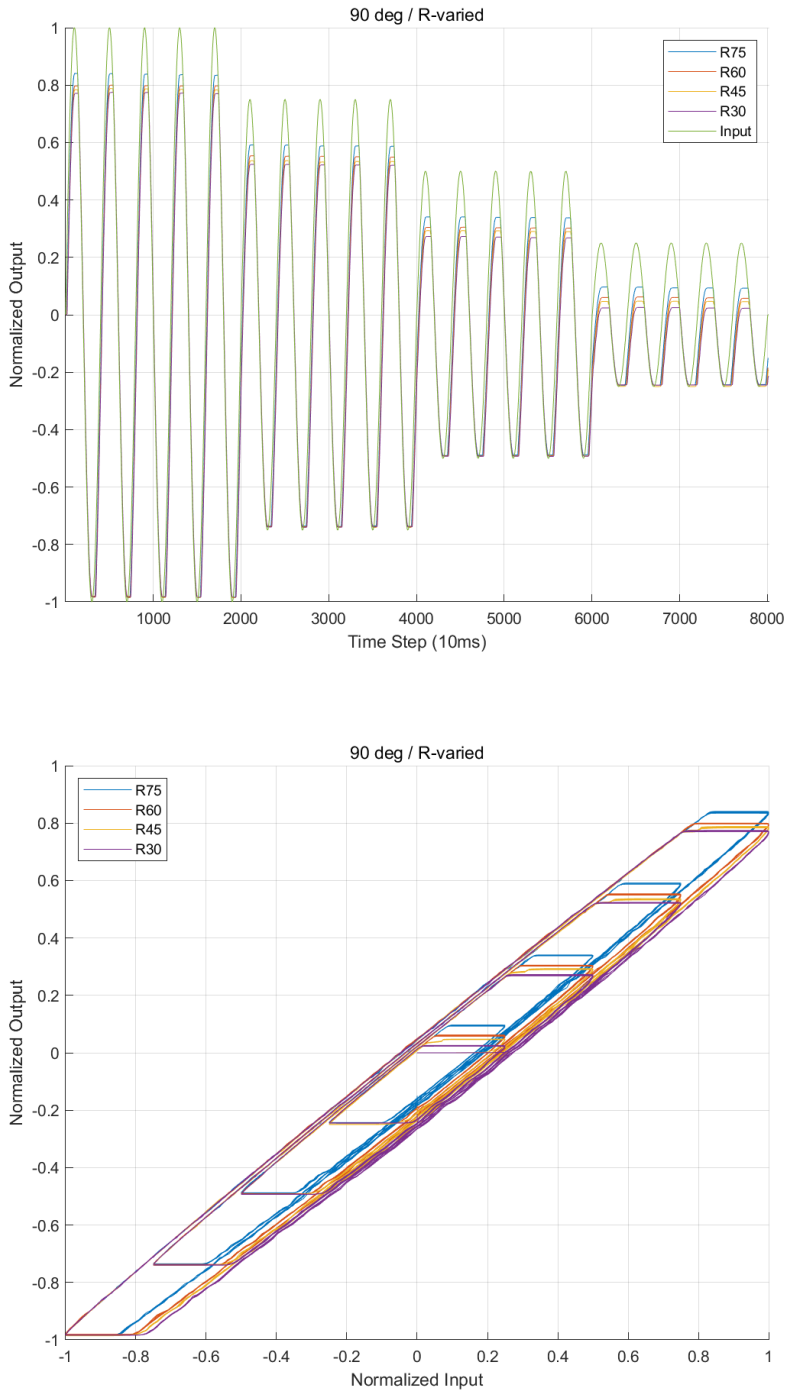


Fig. 3.19 Experiment results for $\phi = 90^{\circ}$ : (a)Output and input measurements for different curve angles, (b) Input-output map for different curve angles

### 3.2.3. Summary of results of hysteretic behavior

As expected, when the curve angle is varied, it affects the output of the TSM. Considering the figures Fig. 3.8 to Fig 3.11, it appears that the hysteretic behavior is intensified as the curve angle increases. When the sinusoidal excitation with decreasing amplitude is provided as an input, it appears that the magnitude has little or no effect on the hysteretic output. Also, at every radius, for the normalized input, the plot shows that the degree of hysteresis, namely the attenuation of diminished magnitudes of output level appears to be similar. This is better shown in Fig. 3.18, where the one period measurement of output at all curve angles is sampled at one period excitation of decreasing sinusoidal excitation input signal with 4.5mm amplitude. Considering Fig. 3.19 we can conclude that the varying curve angle has a greater effect than varying radius of curvature in that in the range that the TSM was experimented, the approximate hysteresis curves at all radii is similar.

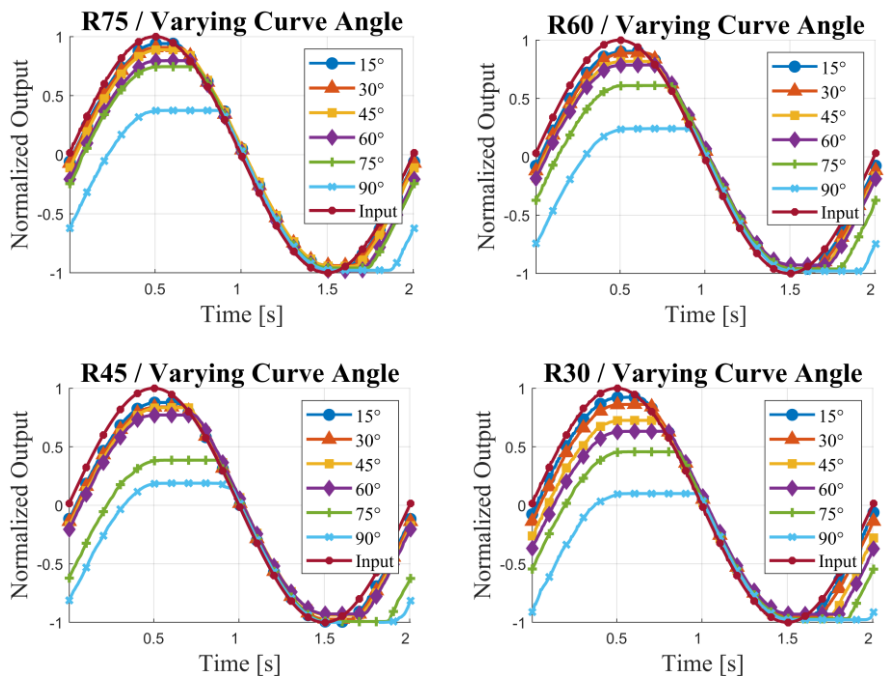


Fig. 3.20 Comparison of sampled output measurements at 4.5mm amplitude – varying curve angle

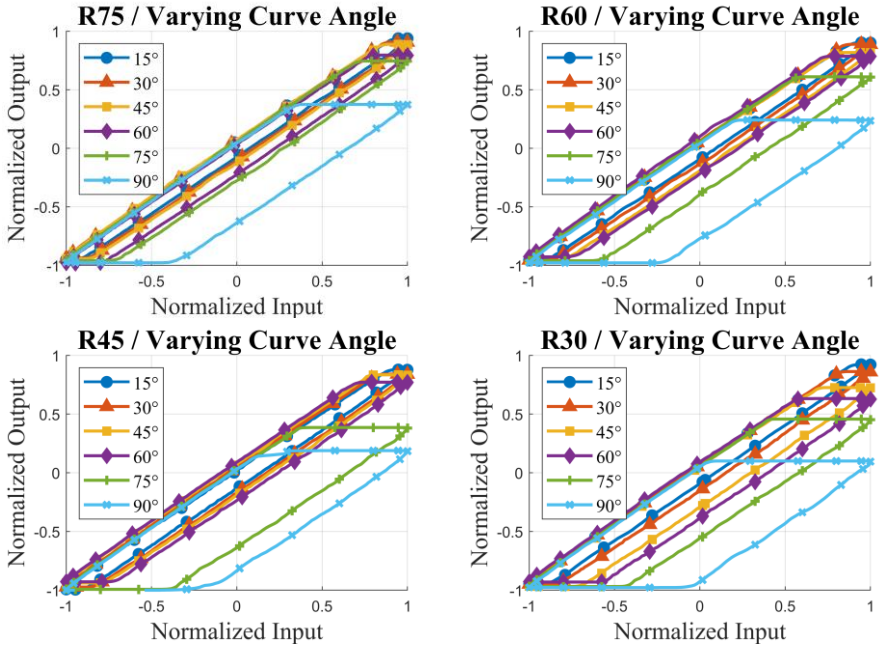


Fig. 3.21 Comparison of input-output map of sampled measurements at 4.5mm amplitude – varying curve angle

In the case of varying radius of curvature, as shown in Fig. 3.12 to Fig. 3.17, we can see immediately that in smaller curve angles, the radius of curvature does not affect the hysteretic output. In greater curve angles however, as the radius of curvature is decreased, the effect is different from that observed from the smaller angles. The hysteretic behavior intensifies as the radius of curvature is decreased in greater curve angles, whereas in smaller angles the effect is minimal. This is better shown in Fig. 3.19 and Fig. 3.20, where like the comparison of the varying curve angles, the data was sampled for one period at 4.5mm amplitude in the decreasing amplitude sinusoidal excitation.

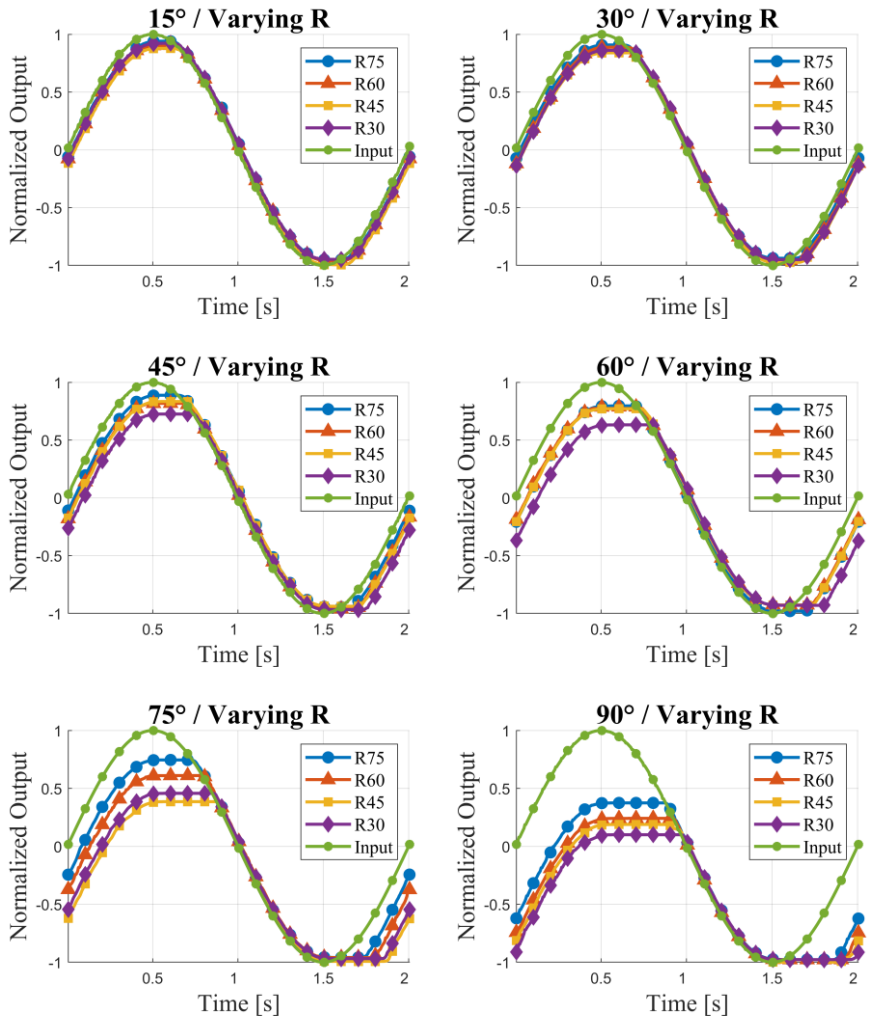


Fig. 3.22 Comparison of sampled output measurements at 4.5mm amplitude – varying curve angle – varying radius of curvature

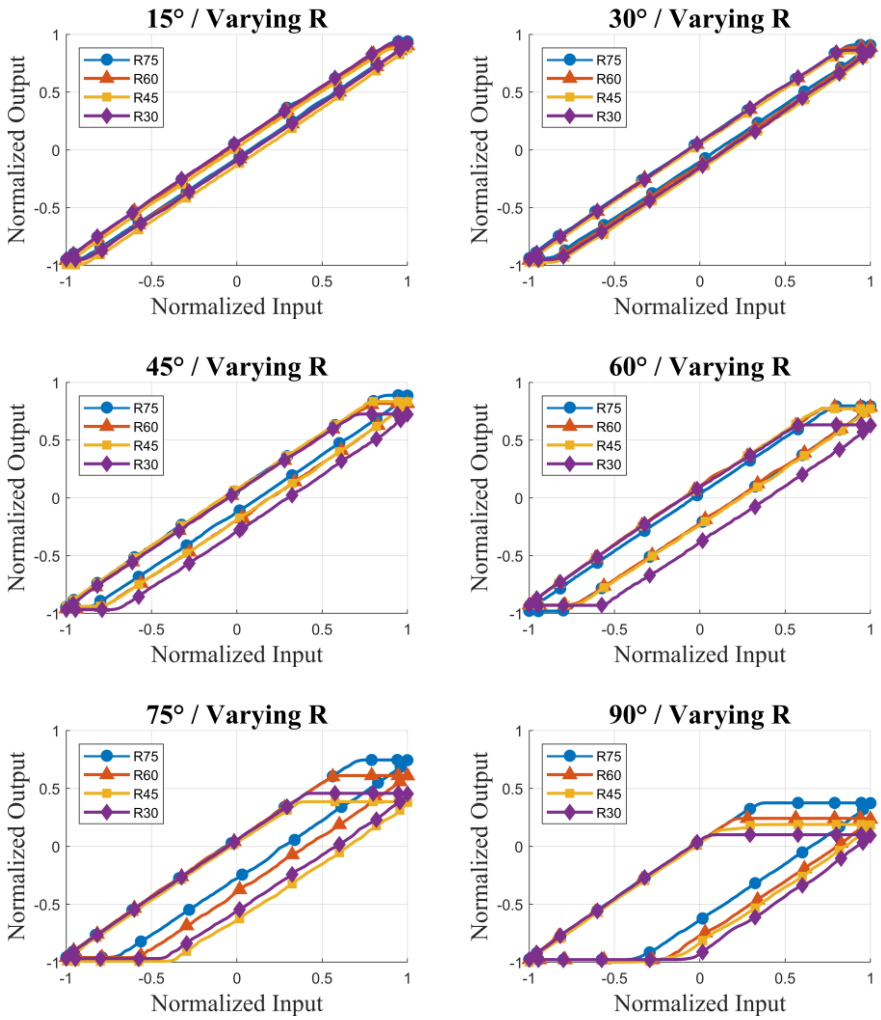


Fig. 3.23 Comparison of input-output map of sampled measurements at 4.5mm amplitude – varying radius of curvature

# Chapter 4. Modeling hysteresis of TSM

## 4.1 Preisach model and hysterons

In this section, the Preisach hysteresis model will be introduced. Preisach model was first suggested in 1935 by Ferenc Preisach. Such model was first proposed to be used in the field of ferromagnetism, as the Preisach model describes a ferromagnetic material as the parallel connection of independent relay hysterons.

Let $\alpha, \beta \in \mathbb{R}$ and $\alpha \le \beta$, then an operator $r_{\alpha,\beta}[\bullet]$ maps $x(t) \mapsto y(x,t)$, where $x(t), y(t)$ are input and output respectively. Then, for $x(t)$ measurable in $[0,T]$, and $y(t) = \zeta$, where $\zeta = \{-1, +1\}$ the initial output $y(0)$ is expressed as the following:

$$y(0) = \begin{cases} 1 & if\ x(t) \ge \alpha \\ -1 & if\ x(t) \le \beta \\ \zeta & if\ \alpha < x(t) < \beta \end{cases} \tag{4.1}$$

When $A_t = \{t \in [0,T] : x(t) = \alpha\ or\ \beta\}$ then the operator $r_{\alpha,\beta}[x(t)]$ is expressed as the following:

$$r_{\alpha,\beta}[x(t)] = y(t) = \begin{cases} y(0) & if\ \ A_t = 0 \\ 1 & if\ \ A_t \ne 0\ \ and\ \ x(\max(A_t = \beta)) \\ -1 & if\ \ A_t \ne 0\ \ and\ \ x(\max(A_t = \alpha)) \end{cases} \tag{4.2}$$

Such operator is called a Nonideal Relay Operator [30], and its plot is shown in Fig. 4.1.

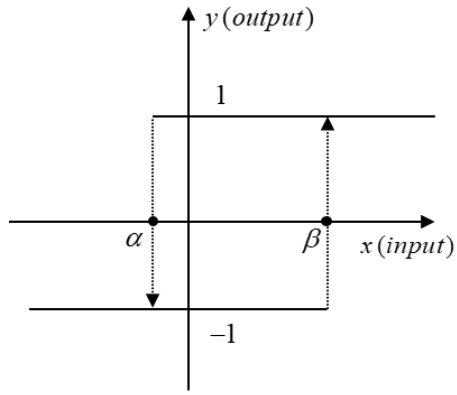


Fig. 4.1 The Nonideal Relay Operator

Based on the nonideal relay operator, a Preisach hysteresis model, $R[x(t)]$ which maps the input $x(t)$ to output $y(t)$ can be constructed as below [31].

$$R[x(t)] = y(t) = \iint (\alpha, \beta) r_{\alpha,\beta}[x(t), y(0)] d\alpha d\beta \tag{4.3}$$

Where $\mu(\alpha, \beta)$ is a Preisach density function, which parameters are empirically identified, and the expression $(\alpha, \beta) r_{\alpha,\beta}[x(t), y(0)]$ is referred to as hysterons, a building block of Preisach hysteresis model. Examples of the widely used Preisach density function is presented in equations (4.4),(4.5),(4.6) which are called Factorized-Lorentzian distribution function, Gauss-Gauss distribution function and Lognormal-Gauss distribution function respectively, which are widely used in modeling hysteresis in structural elements, shape memory alloys and piezo actuators etc.

$$\mu(\alpha, \beta) := N[1 + (\frac{\alpha - H_0}{\sigma \cdot H_0})^2]^{-1}[1 + (\frac{\beta + H_0}{\sigma \cdot H_0})^2]^{-1} \tag{4.4}$$

$$\mu(\alpha,\beta) := N \exp[-\frac{(\frac{\alpha-\beta}{2}-H_0)^2}{2\sigma^2 \cdot {H_0}^2}]\exp[-\frac{(\frac{\alpha+\beta}{2})^2}{2\sigma^2 \cdot {H_0}^2}] \quad (4.5)$$

$$\mu(\alpha,\beta) := N(\frac{2}{\alpha-\beta})\exp[-\frac{\ln(\frac{\alpha-\beta}{2H_0})}{2\sigma^2}]\exp[-\frac{(\alpha+\beta)^2}{8\sigma^2 \cdot {H_0}^2}] \quad (4.6)$$

## 4.2 Mechanical play operator

Extended on the nonideal relay operator in the previous section, a mechanical play operator, $w(t) = f_p\ [v(t), w(t_i)]$, for $t_i < t \le t_{i+1}$, $0 \le i \le N-1$ which maps input $v(t)$ to output $w(t)$ is proposed. Note that the operator $f_p$ takes in the state of $w(t_i)$. Such operator in continuous form, is expressed formally as below:

$$f_p[v, w] = \max\{v, \min\{v + p, w\}\} \tag{4.7}$$

The essence of the operator $f_p$ is depicted in Fig. 4.2 and Fig. 4.3. Fig 4.2 shows the input $v(t)$ to output $w(t)$ map which is also called a Preisach plane. The $p$ is called a mechanical play which, up to a play amount $p$ ,the output is unchanged, but when it reaches the threshold it will follow the input profile. This is best shown in Fig. 4.3 which captures the operator's behavior as a simple piston and cylinder physical model.

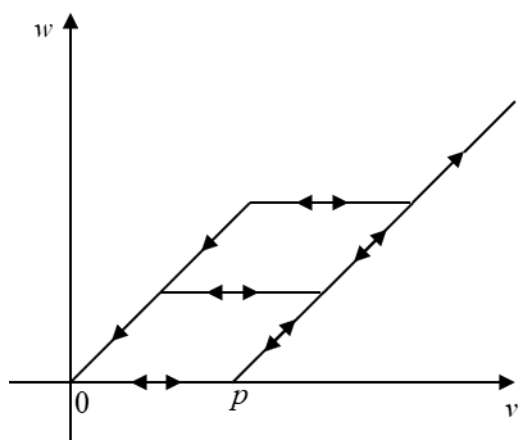


Fig. 4.2 Input-output map of operator $f_p$

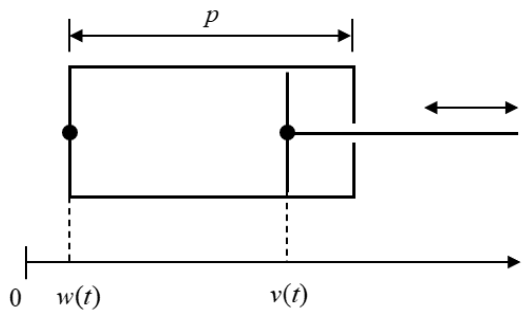


Fig. 4.3 Physical model of operator $f_p$

For discretization of the model, consider a map $v(t) \mapsto w(v,t)$ where $v(t)$ is input and $w(t)$ is output. We define a discretized operator $\gamma$ as below:

$$w(t) = \gamma\ [v(t), w(t_0), v(t_0), p] \tag{4.8}$$

In discrete time domain where $k$ is strictly increasing: $k+1 > k.\ k = 1, 2, \cdots, n$ and setting the initial conditions, $v(t_0) = v(k=1) = w(t_0) = w(k=1) = 0$, as shown in a physical model depiction in Fig. 4.4, we can define an operator $\gamma[v(k), w(k-1), p] = w(k)$ as follows:

$$\gamma\ [v(k), w(k-1), p] = \begin{cases} v(k) & if\ \ w(k\text{-}1) > v(k) \\ w(k\text{-}1) & if\ \ w(k) \le v(k) \le w(k) + p \\ v(k)\text{-}\ p & if\ \ w(k) + p < v(k) \end{cases} \quad for\ k = 2, \cdots, n \tag{4.8}$$

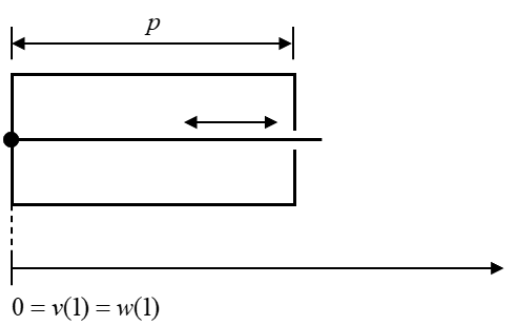


Fig. 4.4 Initial condition of operator $\gamma$

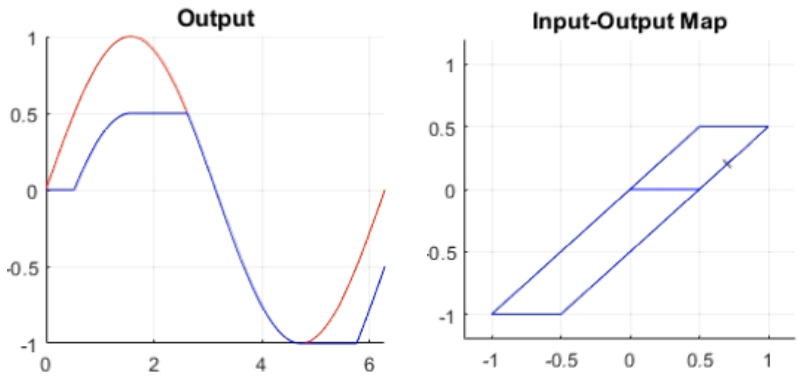


Fig. 4.5 Output and input-output map of operator $\gamma$

The output of a $\gamma$ operator when the input $v(t)$ is sin(t) and the mechanical play $p = 0.5$ is shown in Fig. 4.5.

## 4.3 Complex hysteresis operator: Γ

Analogous to the hysterons and Preisach hysteresis model, the discretized mechanical play operator $\gamma$ can be extended in a way that linearly superpositioning the mechanical play operators $\gamma$ with different play amount $p$ and the contributing weight of each operator to the total sum of operators. When $n$ is the number of mechanical play operators $\gamma$, or also denoted as degree-of-freedom (DOF), with initial conditions $v(k=1)=w_i(k=1)=0$ where $i$ denotes the distinct operator $\gamma_i$ of the $n$ number of operators, we can define a combined complex output $w_c(k)$ as follows, which is denoted $\Gamma_n$:

$$w_c(k) = \Gamma_n \left[v(k), \mathbf{P}, \mathbf{Q}, \mathbf{W}_{k-1}\right] = \sum_{i=1}^{n} q_i \gamma_i \left[v(k), w_i(k-1), p_i\right] \text{ for } k = 2,3,\cdots n \quad (4.9)$$

Where $\gamma_i$ is an elementary mechanical play operator defined in the previous section, $q_i$, $p_i$ are the weight of each $\gamma_i$ and play amount for each $\gamma_i$ respectively, $w_i(k-1)$ is the $(k-1)^{th}$ output of each $\gamma_i$ and $v(k)$ is the current input at step k. $\mathbf{P}=(p_1,\cdots p_n)$ is a vector of play thresholds, $\mathbf{Q}=(q_1,\cdots q_n)$ is a vector of weights, and $\mathbf{W}_{k-1}=(w_{1,k-1},\cdots w_{n,k-1})$ is a vector of $(k-1)^{th}$ output of each $\gamma_i$. The structure of a discretized complex hysteresis operator $\Gamma$ with $n$ degree-of-freedom is visualized in Fig. 4.6.

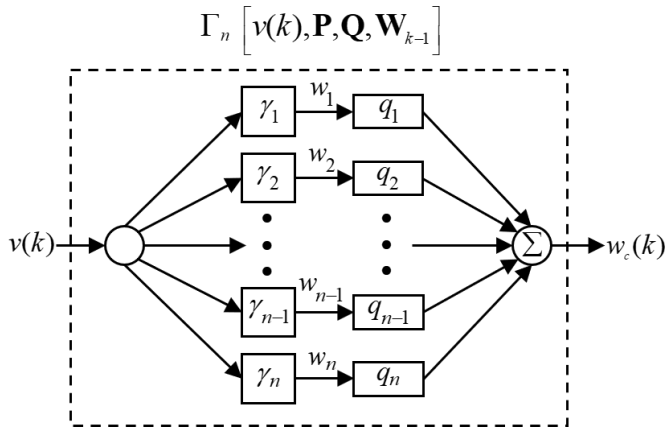


Fig. 4.6 Structure of complex hysteresis operator of $n$ DOF, $\Gamma_n$

In essence, the $\Gamma$ operator is a weighted sum of elementary operators $\gamma$, that have distinct play amounts $p$. The power of utilizing such operator is in its ability to model hysteresis curves with relatively small number of elementary operators $\gamma$ or equivalently, small number of DOF. As shown in Fig. 4.7, with 10 DOF and $\mathbf{P}=(p_1,\cdots p_n)=(0,0.1,0.2,0.3,0.4,0.5,0.6,0.7,0.8,0.9)$ with equal weights of each $\gamma_i$ with $\mathbf{Q}=(q_1\cdots q_n)=(0.1,0.1,0.1,0.1,0.1,0.1,0.1,0.1,0.1,0.1)$ it can be seen that it is able to model the nonlinear hysteresis curves with relatively small number of elements.

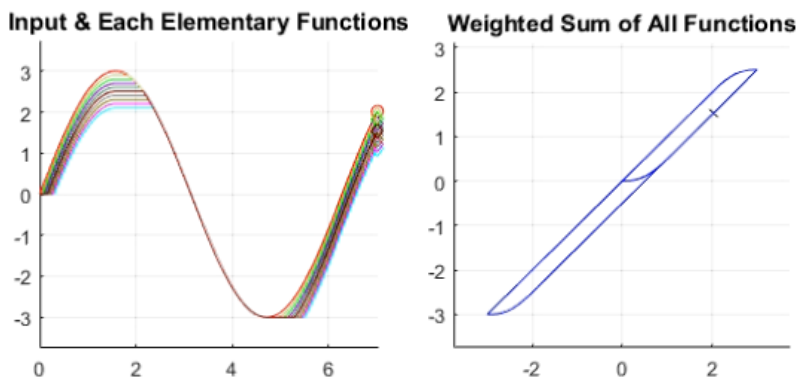


Fig. 4.7 Output and input-output map of operator $\Gamma_{10}$ with equal weights and $\mathbf{P}=(0,0.1,0.2,\cdots,0.9)$

The weights in the shown example of $\Gamma_{10}$ in Fig. 4.7 have all positive values, but if we expand the range of weights to have negative values as well, the complex hysteresis operator is able to describe wide variety of hysteresis curves. The $\mathbf{P}$ vector, the play amounts for each $\gamma_i$, has to be set considering the magnitude of the hysteresis. If the $\mathbf{P}$ vector is set improperly, then no linear combinations of $\gamma_i$, or weights, may be found to describe the hysteretic system of interest. A general rule of thumb is to set the sum of play amounts, that is $\mathbf{PP^T}$, to be at least twice the amount of hysteresis magnitude.

## 4.4 Parameter identification for complex hysteresis operator

To empirically model the TSM's hysteretic output with the proposed model as described in the previous section, the weight vector $\mathbf{Q}$ has to be identified. Identification of $\mathbf{Q}$ with respect to the measured output of the TSM at 24 different shape configurations is an optimization problem that minimizes the function of $\mathbf{Q}$. The formulation of optimization problem is shown in equations (4.10)

$$
\begin{aligned}
&\textit{given} && n,\ \mathbf{P} = (p_1, \ldots, p_n),\ v(k),\ k = 1, 2, \cdots N \\
&\textit{minimize} && f(\mathbf{Q}) = \left\| \mathbf{w}_c - \mathbf{w}_{measured} \right\|^2 \\
& && = \sum_k \Big( \sum_{i=1}^{n} q_i \gamma_i \ \left[ v(k), w_i(k-1), p_i \right] - w_{measured,k} \Big)^2 \\
&\textit{subject to} && \mathbf{Q}\mathbf{Q}^{\mathrm{T}} = 1 \\
& && \mathbf{W}_{k-1}(1) = (0, \cdots, 0)
\end{aligned}
\tag{4.10}
$$

The optimization problem minimizes the quadratic error term $\left\| \mathbf{w}_c - \mathbf{w}_{measured} \right\|^2$, which is a function of weight vector $\mathbf{Q}$. $\mathbf{w}_c$ is the combined output of complex hysteresis operator $\Gamma_n$, and $\mathbf{w}_{measured}$ is the measured data of TSM output. $n$ is the number of elementary operators $\gamma$ ,or degree-of-freedom, which is determined beforehand. The quadratic error term is propagated to all the measured data points at $k^{th}$ step. $\mathbf{P}$ is the preassigned play amounts for each elementary operators $\gamma$. The condition $\mathbf{Q}\mathbf{Q}^{\mathrm{T}} = 1$ imposes a constraint of the sum of all weights for elementary operators that is equal to 1. Finally the condition $\mathbf{W}_{k-1}(1) = (0, \cdots, 0)$ imposes a constraint for the very first point in optimization, as each $\gamma$ operator need a previous state $w_i(k-1)$ . For the optimization algorithm, the interior point algorithm

implemented in Matlab FMINCON function was used to solve the optimization problem.

The measured reference $\mathbf{w}_{measured}$ ,for solving for $\mathbf{Q}$ is obtained from the sinusoidal excitation of decreasing amplitude with 6mm,4.5mm,3mm,1.5mm with 5 periods at each amplitudes, shown in Fig. 4.8. At all 24 different combinations of shape configurations, such sinusoidal excitation was provided as an input and the output displacement was measured with an optical encoder. Verification of model was performed by applying the model with the obtained $\mathbf{Q}$, to predict the outputs of triangular wave and trapezoidal wave of input as shown in Fig. 4.9. Both the triangular and trapezoidal wave is generated so that the slope, or velocity, is 6mm/s. The predicted output and the actual measured output from triangular and trapezoidal wave were compared to establish the validity of the model. For the TSM configured in this research, considering the hysteresis curve observed in the previous section the degree-of-freedom, or $n$ is set to be 11. For the play amounts of each operator $\gamma_i$, $\mathbf{P} = (0, 0.2, 0.4, 0.6, 0.8, 1.0, 1.2, 1.4, 1.6, 1.8, 2.0)$ was preassigned for the optimization.

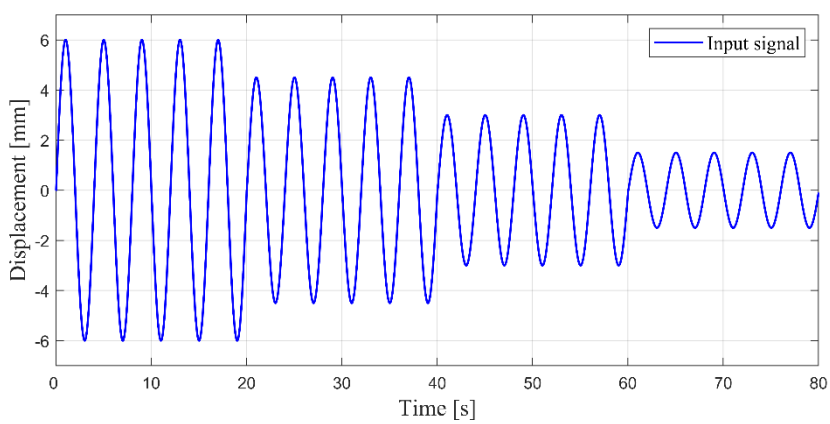


Fig. 4.8. Decreasing sinusoidal excitation used for obtaining $\mathbf{Q}$

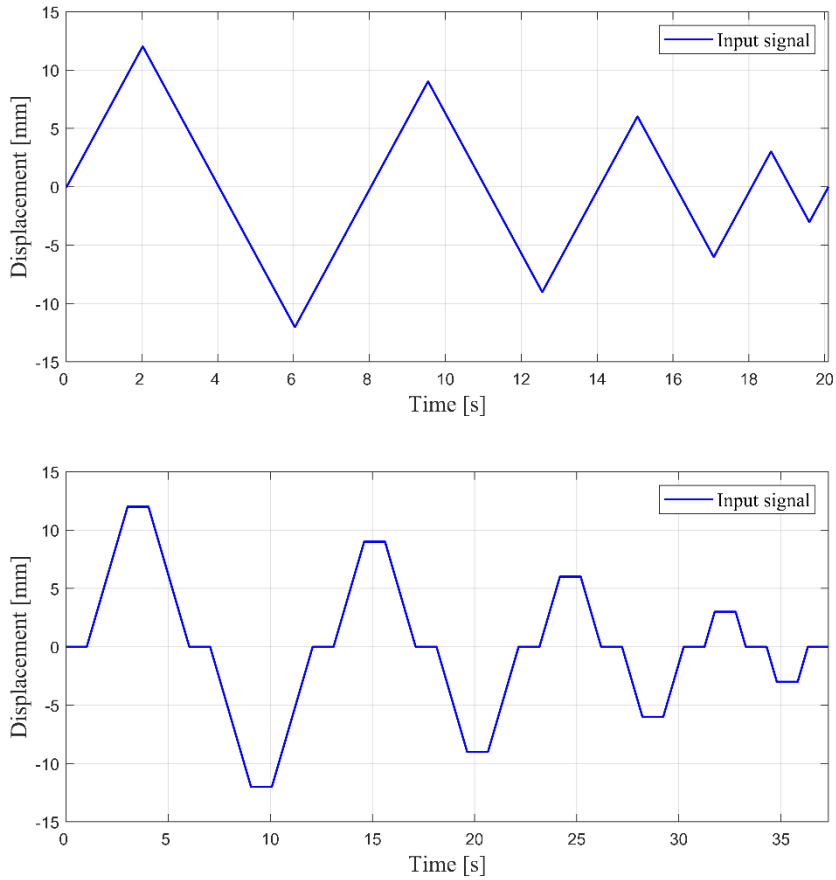


Fig. 4.9 Input signals for validation of model: (a)triangular, (b)trapezoidal

## 4.5 Result of experimental verification of complex hysteresis operator

24 sets of weight vector $\mathbf{Q}$ for 24 different shape configurations were obtained. In this section the exemplary shape of $\phi = 90^{\circ}, r = 30mm$ out of 24 shape configurations is presented. As discussed in the previous section, the sinusoidal excitation in which the weight $\mathbf{Q}$ was obtained from will be compared to the model estimated output and the measured output. Then the results of validation set, triangular wave and trapezoidal wave, will be presented. For all of the input profiles the combined output $\mathbf{w}_c$ is compared to the measured output, and the measured input-output map will be overlaid on the model input-output map. Also the elementary operators with the weight multiplied, which is analogous to the hysterons in Chapter 4.1, will be presented to show how elementary operators are superpositioned to generate a complex hysteresis model. Lastly, the weights of all 24 models for distinct shape configurations and the sum of squared errors (SSE) will be presented.

### 4.5.1 Result of reference input profile – sinusoidal excitation

As previously discussed the degree-of-freedom of the complex hysteresis operator $n$ was set to 11, and the corresponding $\mathbf{P}$ were predetermined. The optimization result of obtaining $\mathbf{Q}$ is presented below

$$\begin{aligned}
&\phi = 90^{\circ}, r = 30mm \\
&n = 11 \\
&\mathbf{P} = (p_1, \cdots, p_n) = (0, 0.2, 0.4, 0.6, 0.8, 1.0, 1.2, 1.4, 1.6, 1.8, 2.0) \\
&\mathbf{Q} = (q_1, \cdots, q_1) = (-0.333, 0.422, 0.056, 0.798, 0.031, 0.006, \\
&\qquad\qquad -0.019, 0.066, -0.226, 0.649, -0.473)
\end{aligned} \tag{4.11}$$

The corresponding results for sinusoidal excitation are presented in Fig. 4.10. Fig. 4.11, Fig. 4.12, Fig. 4.13.

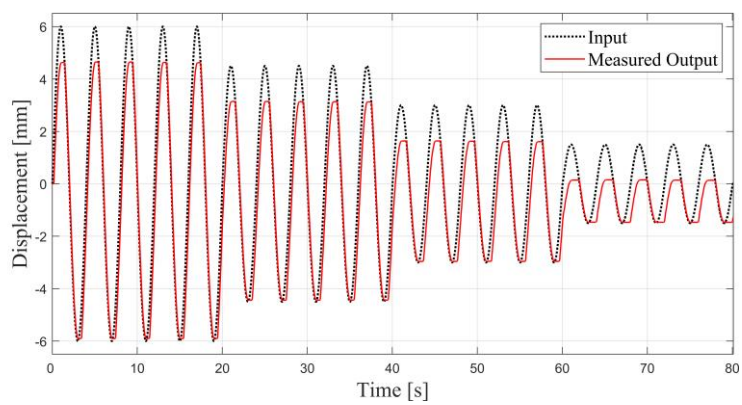


Fig. 4.10 Input and output measurements of $\phi = 90^{\circ}, r = 30mm$ shape – sinusoidal excitation

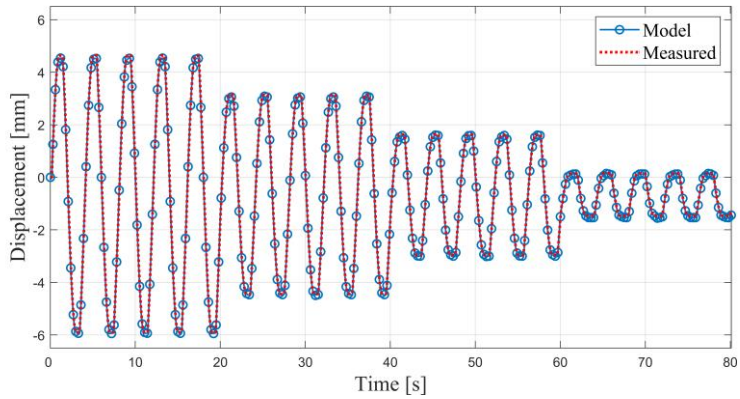


Fig. 4.11 Model and measured output of $\phi = 90^{\circ}, r = 30mm$ shape – sinusoidal excitation

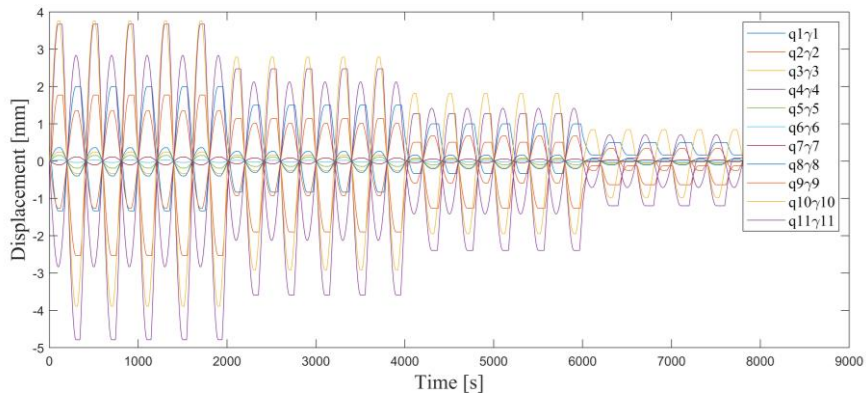


Fig. 4.12 Elementary $q_i \gamma_i$ 's of $\Gamma$ for $\phi = 90^{\circ}, r = 30mm$ shape – sinusoidal excitation

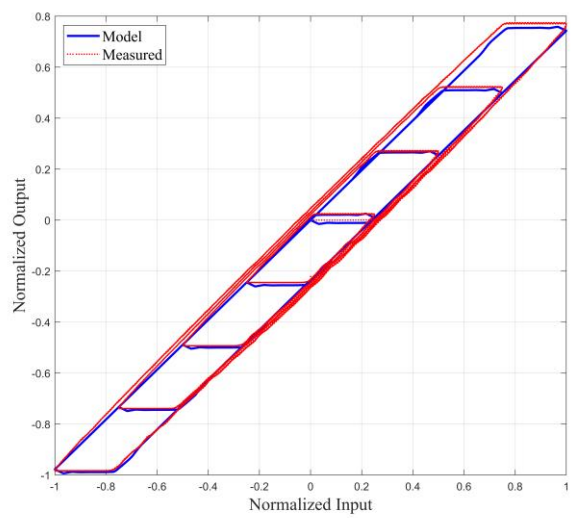


Fig. 4.13 Input-output map of model estimated output and measured output for $\phi = 90^{\circ}, r = 30mm$ shape-sinusoidal excitation

### 4.5.2 Result of validation input profile– triangular excitation

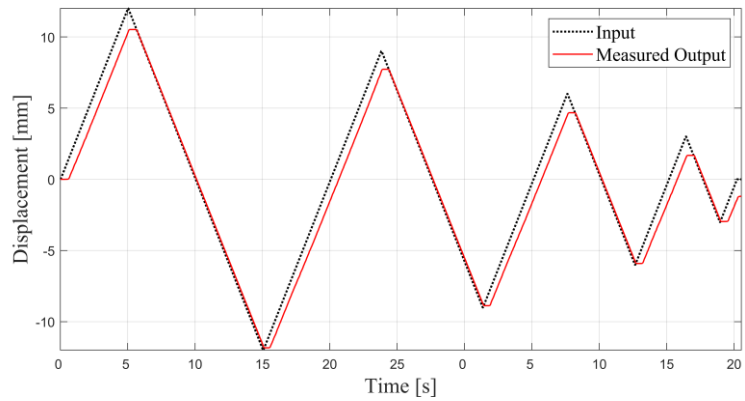


Fig. 4.14 Input and output measurements of $\phi = 90^{\circ}, r = 30mm$ shape – triangular excitation

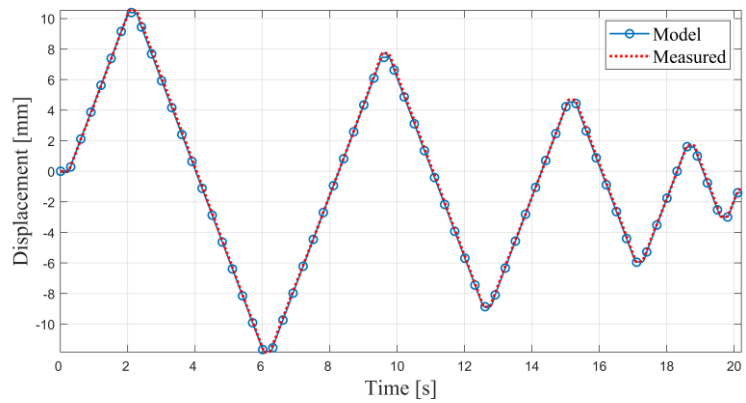


Fig. 4.15 Model and measured output of $\phi = 90^{\circ}, r = 30mm$ shape – triangular excitation

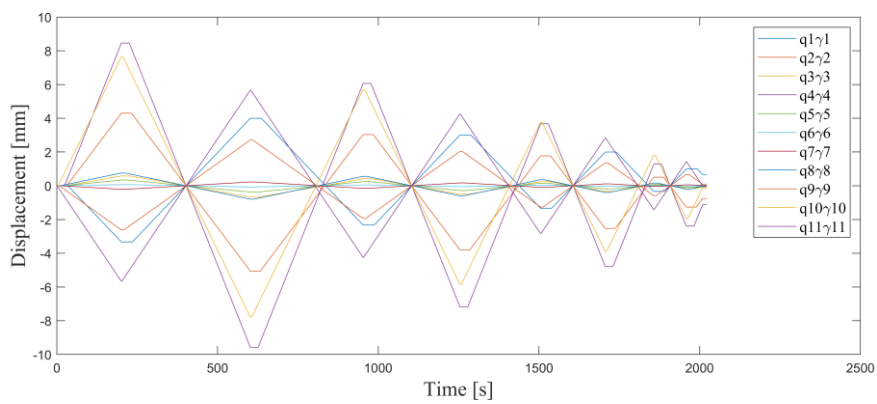


Fig. 4.16 Elementary $q_i \gamma_i$ 's of $\Gamma$ for $\phi = 90^{\circ}, r = 30mm$ shape – triangular excitation

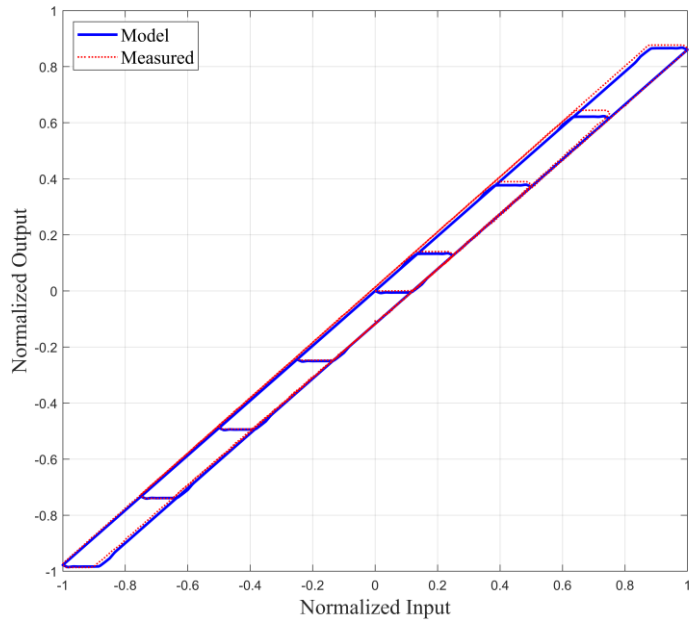


Fig. 4.17 Input-output map of model estimated output and measured output for $\phi = 90^{\circ}, r = 30mm$ shape– triangular excitation

### 4.5.3 Result of validation input profile– trapezoidal excitation

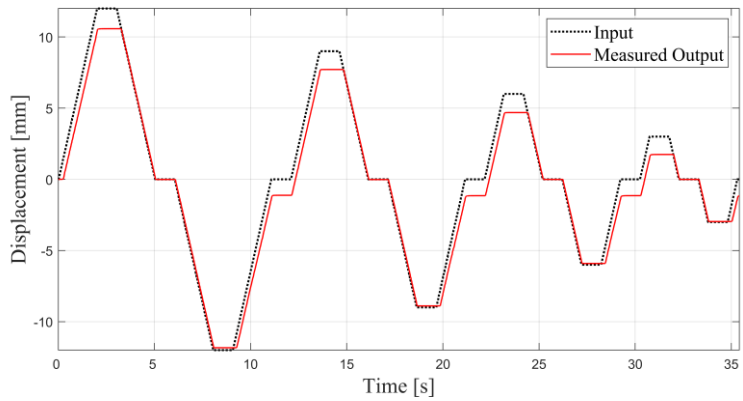


Fig. 4.18 Input and output measurements of $\phi = 90^{\circ}, r = 30mm$ shape – trapezoidal excitation

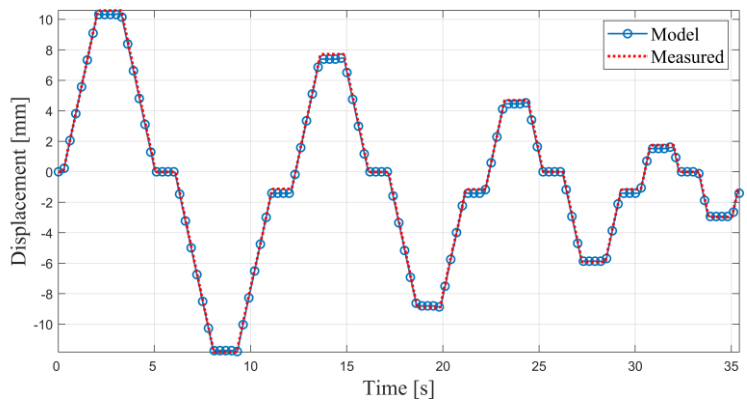


Fig. 4.19 Model and measured output of $\phi = 90^{\circ}, r = 30mm$ shape – trapezoidal excitation

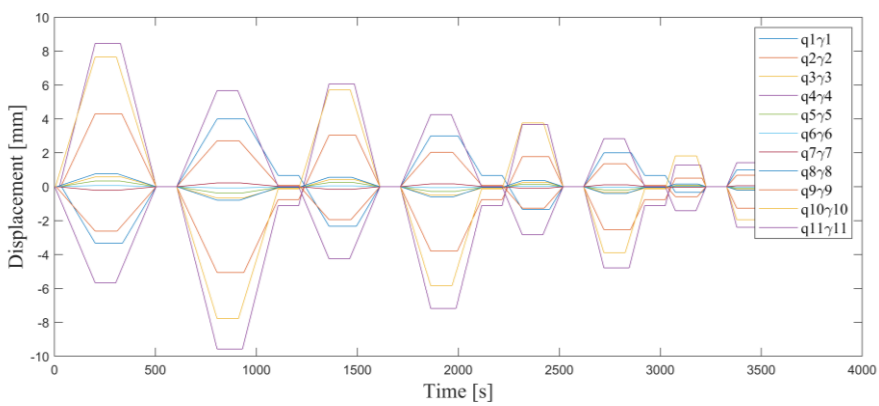


Fig. 4.20 Elementary $q_i \gamma_i$ 's of $\Gamma$ for $\phi = 90^{\circ}, r = 30mm$ shape – trapezoidal excitation

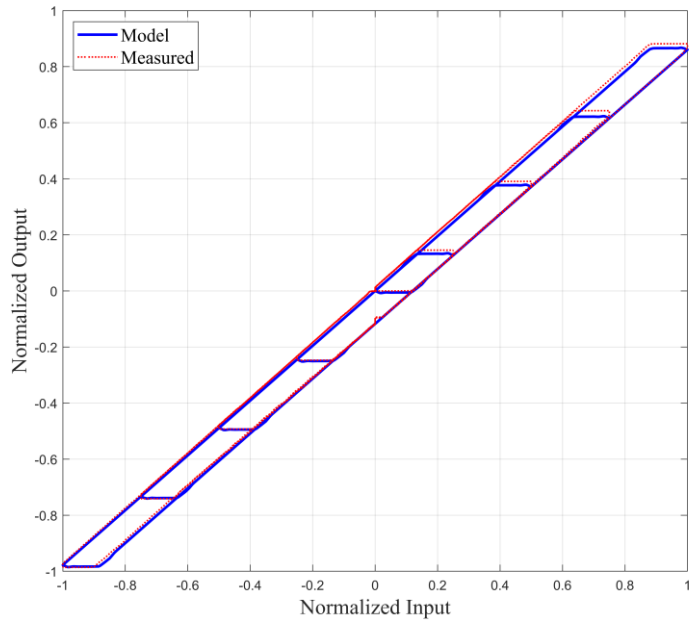


Fig. 4.21 Input-output map of model estimated output and measured output for $\phi = 90^{\circ}, r = 30mm$ shape– trapezoidal excitation

### 4.5.4 Obtained weights for all shape configurations and summary

The obtained **Q** vector for all 24 distinct shapes are tabularized in Table 4.1, along with the sum of squared errors for each shapes when modeled with such **Q**. Highlighted shape is the exemplary shape that was presented in the previous sections.

Table 4.1 Weight vector **Q** for all shape configurations and SSE

| $\phi$ | $r$ | $Q$ | $\|w_c - w_{desired}\|^2$ |
|---|---|---|---|
| 15° | 30mm | (-0.647, 0.871, -0.253, 0.006, 0.068, -0.060, 0.063, -0.002, -0.099, 1.144, -0.119) | 50.84 |
| | 45mm | (-0.265, 0.372, -0.099, -0.015, 0.068, -0.052, 0.023, 0.058, -0.208, 1.339, -0.239) | 26.48 |
| | 60mm | (-0.547, 0.730, -0.205, 0.043, -0.007, 0.014, -0.015, 0.046, -0.134, 1.156, -0.106) | 44.15 |
| | 75mm | (-0.636, 0.836, -0.209, -0.001, 0.027, 0.018, -0.024, 0.080, -0.216, 1.148, -0.049) | 52.42 |
| 30° | 30mm | (-0.642, 0.828, -0.208, 0.022, -0.011, 0.054, 0.012, -0.071, 0.319, 0.917, -0.249) | 49.00 |
| | 45mm | (-0.473, 0.612, -0.118, -0.024, 0.033, -0.009, 0.023, -0.054, 0.301, 0.973, -0.287) | 35.46 |
| | 60mm | (-0.630, 0.820, -0.198, 0.038, -0.043, 0.042, -0.003, 0.000, 0.075, 1.127, -0.255) | 47.40 |
| | 75mm | (-0.701, 0.899, -0.194, -0.034, 0.061,-0.007, 0.008, 0.015, -0.053, 1.152, -0.176) | 55.55 |
| 45° | 30mm | (-0.504, 0.651, -0.128, -0.020, 0.017, 0.065, -0.121, 0.332, 0.634, 0.318, -0.268) | 37.60 |
| | 45mm | (-0.742, 0.964, -0.241, 0.036, -0.025, 0.036, 0.028, -0.088, 0.703, 0.527, -0.229) | 56.85 |
| | 60mm | (-0.527, 0.666, -0.133, 0.002, 0.022, -0.010, 0.027, -0.061, 0.513, 0.782, -0.306) | 43.01 |
| | 75mm | (-0.721, 0.932, -0.218, 0.018,-0.008, 0.039, -0.020, -0.032, 0.177, 1.042, -0.238) | 57.21 |
| 60° | 30mm | (-0.764, 1.007, -0.256, 0.016, 0.079, -0.108, 0.183, 0.853, -0.103, 0.221, -0.155) | 54.19 |
| | 45mm | (-0.805, 1.041, -0.259, 0.030, -0.002, 0.004, -0.025, 0.207, 0.757, 0.130, -0.109) | 58.86 |
| | 60mm | (-0.810, 1.051, -0.276, 0.050, 0.008, -0.006, -0.032, 0.136, 0.778, 0.224, -0.156) | 60.55 |
| | 75mm | (-0.397, 0.519, -0.098, -0.019, 0.036, -0.028, 0.040, -0.066, 0.551, 0.789, -0.348) | 31.05 |
| 75° | 30mm | (-0.516, 0.687, -0.201, 0.164, -0.236, 0.528, 0.615, -0.051, -0.130, 0.433, -0.318) | 42.94 |
| | 45mm | (-0.354, 0.507, -0.126, 0.097, -0.202, 0.864, 0.220, 0.008, -0.180, 0.544, -0.398) | 32.77 |
| | 60mm | (-0.562, 0.755, -0.203, 0.014, 0.036, -0.063, 0.212, 0.815, -0.109, 0.292, -0.210) | 39.02 |
| | 75mm | (-0.575, 0.735, -0.126, -0.059, 0.059, 0.001, -0.078, 0.305, 0.660, 0.291, -0.237) | 40.39 |
| 90° | 30mm | (-0.333, 0.422, 0.056, 0.798, 0.031, 0.006, -0.019, 0.066, -0.226, 0.649, -0.473) | 42.37 |
| | 45mm | (-0.306, 0.478, -0.202, 0.640, 0.174, 0.189, -0.017, 0.080, -0.260, 0.738, -0.537) | 37.18 |
| | 60mm | (-0.450, 0.676, -0.208, 0.070, 0.875, 0.022, -0.029, 0.072, -0.223, 0.636, -0.464) | 41.60 |
| | 75mm | (-0.413, 0.528, -0.043, -0.026, -0.010, 0.776, 0.180, 0.017, -0.159, 0.473, -0.345) | 35.99 |

The sum of squared error (SSE) for all shape configurations are of sinusoidal excitation. Since the SSE increases as the time series of data increases it would not be suitable to compare for different durations of signal, but in Table 4.1 the results are SSE for comparison of identical sinusoidal input with the duration of 80seconds as shown in Fig. 4.8. The exemplary shape configuration of $\phi = 90^{\circ}, r = 30mm$ has the SSE of 42.37 and the other configurations are commensurate.

## 4.6 Inverse operator formulation

The complexity in implementing a inverse operator for the generation of inverse control signal to compensate for hysteresis is best explained by an physical example shown in Fig. 4.22. Consider a single element operator with a mechanical play amount $p=2$, and initial conditions set to 0 for both input and output. In the first case, when the input at time step $k=2$, reaches 2, output remains unchanged. At time step $k=3$, input moves backward to 1, and the output remain unchanged. If we consider the second case, the initial conditions are same, and the final position for input at time step $k=3$ is same, but the input position at time step $k=2$ is different from the first case. This implies that the discretized hysteresis operator must be provided with not only the current input at time step $k$, but also with either one of the two information, or states: the complete history of input from initial $k=1$ to current time step $k$ or the previous known output at time step $k-1$. Clearly, the latter will be of more efficient choice since the only state that needs to be stored is the last $k-1$ time step's output. This is the memory property of hysteresis operator.

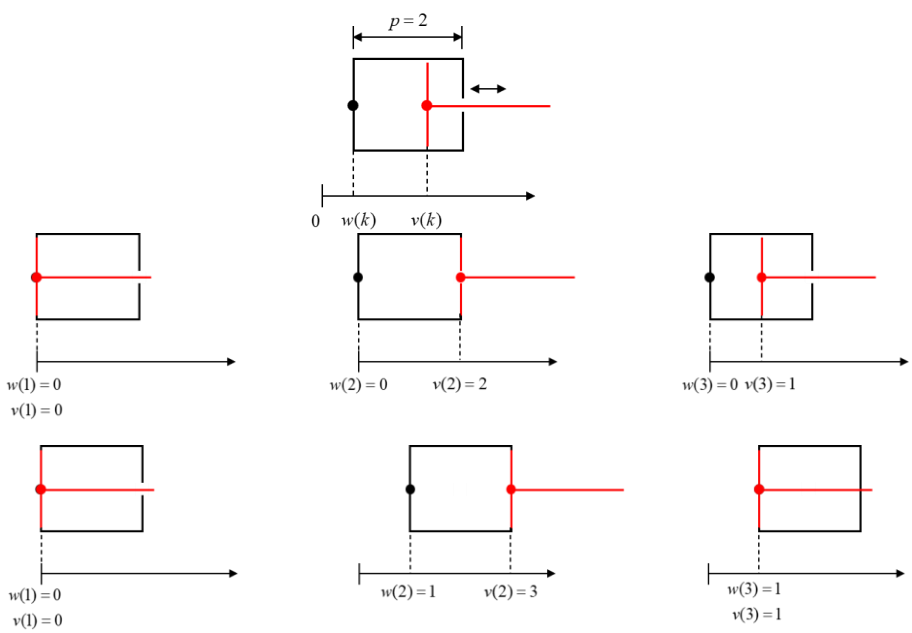


Fig. 4.22 Memory property and the need of states in hysteresis operator

Taking in to account the memory property of the hysteresis operator, a inverse operator $\Gamma_k^{-1}$, at the time step $k$ in the discrete time domain $k=1,2,\cdots,N$ is implemented as shown in Fig. 4.23. $\Gamma_k^{-1}$ processes the desired output $w_{desired,k}$ at the current time step $k$ to produce $v_k$, an inverse control signal that compensates the original hysteretic output of the system.

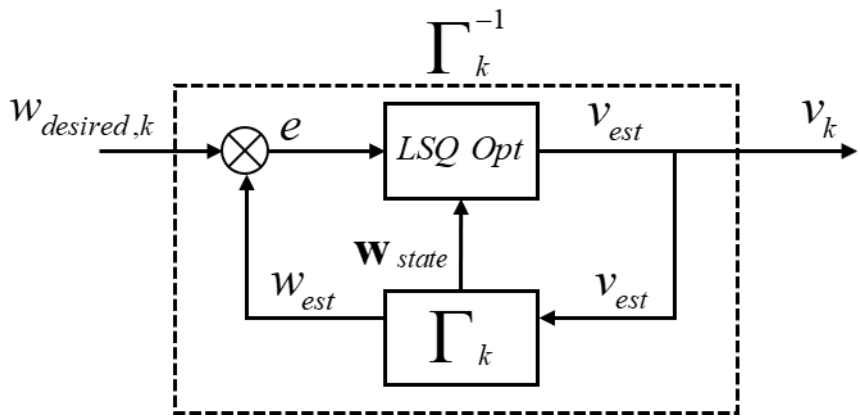


Fig. 4.23 The inverse operator $\Gamma_k^{-1}$ processing the desired output $w_{desired,k}$ to produce an inverse control signal $v_k$ at current time step $k$

As previously stated, the hysteresis operator requires the state of the last time step $k-1$. for complex hysteresis operator $\Gamma$, this is the internal state of all $n$ elementary hysteresis operators, which can be expressed as in the vector form of, $\mathbf{W}_{state}=(w_1,w_2,\cdots,w_n)$. This is depicted in Fig. 4.24.

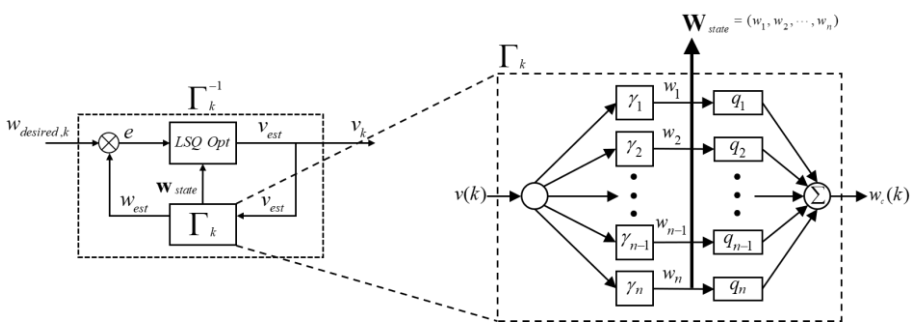


Fig. 4.24 Internal state for the inverse operator $\Gamma_k^{-1}$

The entire algorithmic flow of the inverse operator will be described in step by step fashion. Consider inversion step 1, presented in Fig. 4.25. The first estimate $v_{est}$ is produced by least squares optimization ( $LSQ\,Opt$ ) at an initial point $v_0 = 0$.

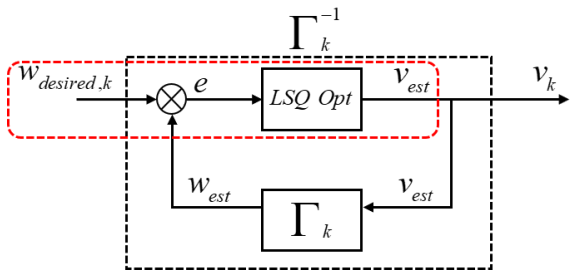


Fig 4.25 Inversion step 1

For the next step shown in Fig. 4.26, the first estimate $v_{est}$ is fed to $\Gamma_k$, and the $\Gamma_k$ needs a previous state vector to produce $w_{est}$.

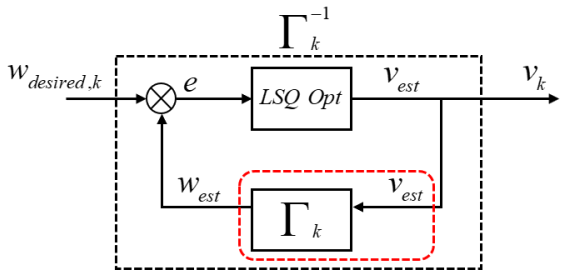


Fig. 4.26 Inversion step 2

For that matter, a last known state vector $\mathbf{W}_{state,k-1}$, from the previous time step $k-1$ is fed to the $\Gamma_k$, as shown in Fig. 4.27, and $w_{est}$ is computed.

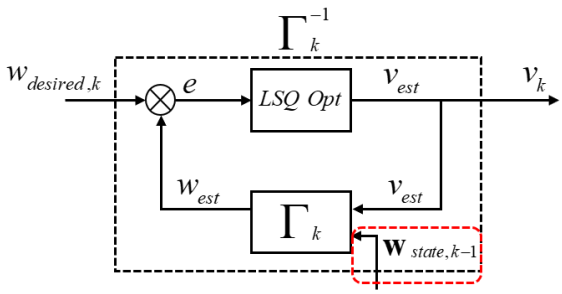


Fig. 4.27 Inversion step 3

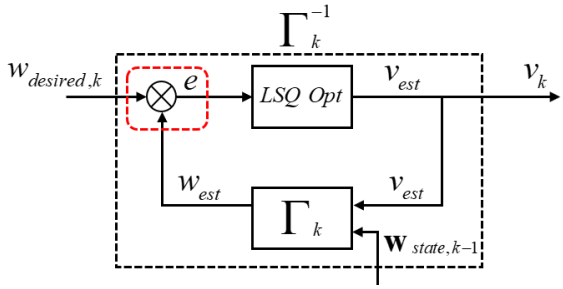


Fig. 4.28 Inversion step 4

Then, as shown in Fig. 4.28, the error $e$ is calculated from $w_{est}$ and $w_{desired,k}$ and the optimization loop of $LSQ\,Opt$ continues until the error is below a predefined threshold.

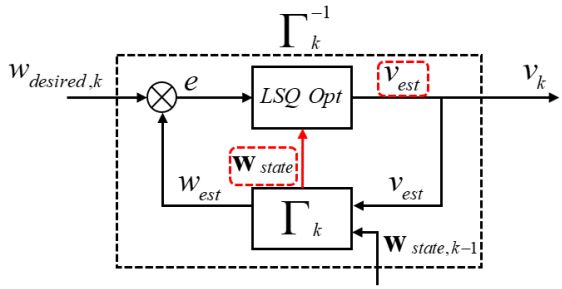


Fig. 4.29 Inversion step 5

At inversion step 3, after the $\Gamma_k$ operator processed $v_{est}$ to produce $w_{est}$, the internal state $\mathbf{W}_{state}$ changes. Hence, this updated state is fed to the $LSQ\,Opt$ loop to produce a better estimate $v_{est}$. Now, when the $LSQ\,Opt$ loop is terminated due to the error reaching below the predefined threshold, the last $v_{est}$ becomes $v_k$, and the last $\mathbf{W}_{state}$ is saved as $\mathbf{W}_{state,k}$ and passed on to the next time step $k+1$ inverse operator, as shown in Fig. 4.30.

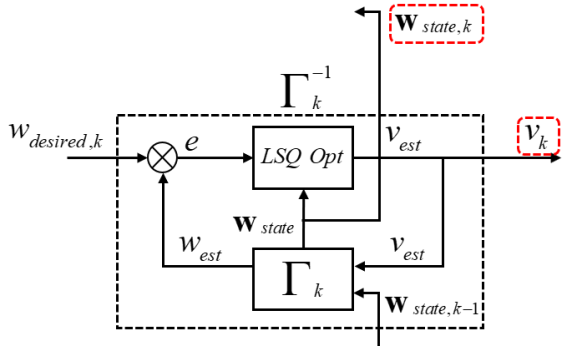


Fig. 4.30 Inversion step 6

Following the inversion steps, the complete recursive algorithm is presented in Fig. 4.31.

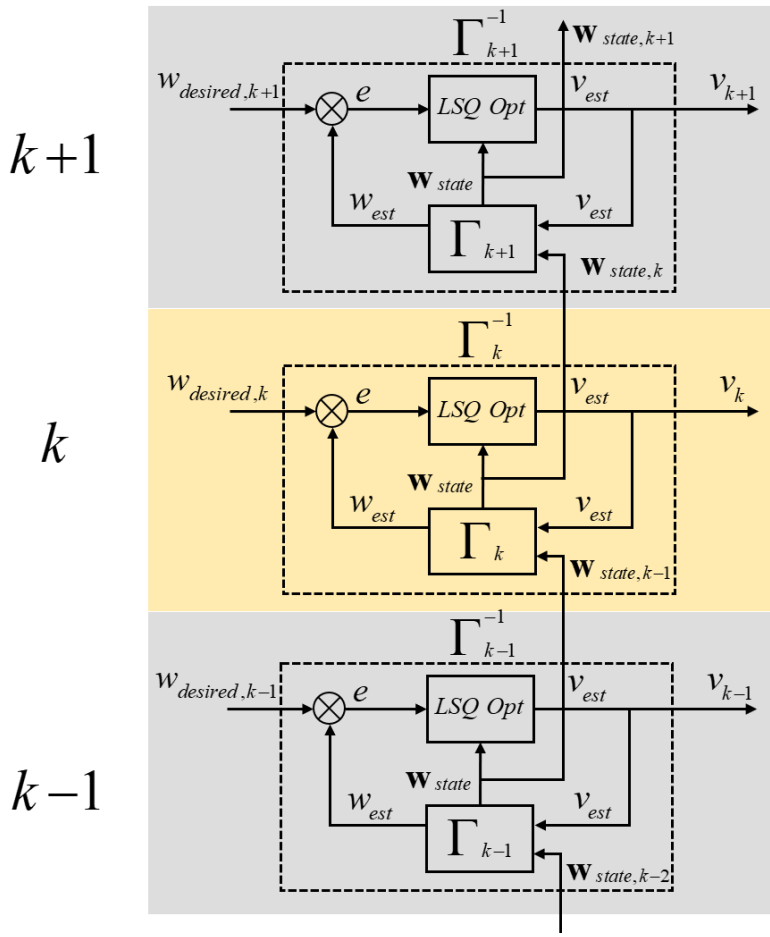


Fig. 4.31 Inversion schematic at time steps $k-1, k, k+1$

For faster conversion of the $LSQOpt$, additional consideration is needed. At inversion step 1, in Fig. 4.25, $LSQOpt$ produces a first estimate from the initial point $v_0 = 0$. But if we set the initial point as the last produced inverse signal from the last time step as shown in Fig. 4.32, the $LSQOpt$ search starts from $v_0 = v_{k-1}$ rather than $v_0 = 0$, resulting in a significantly faster convergence.

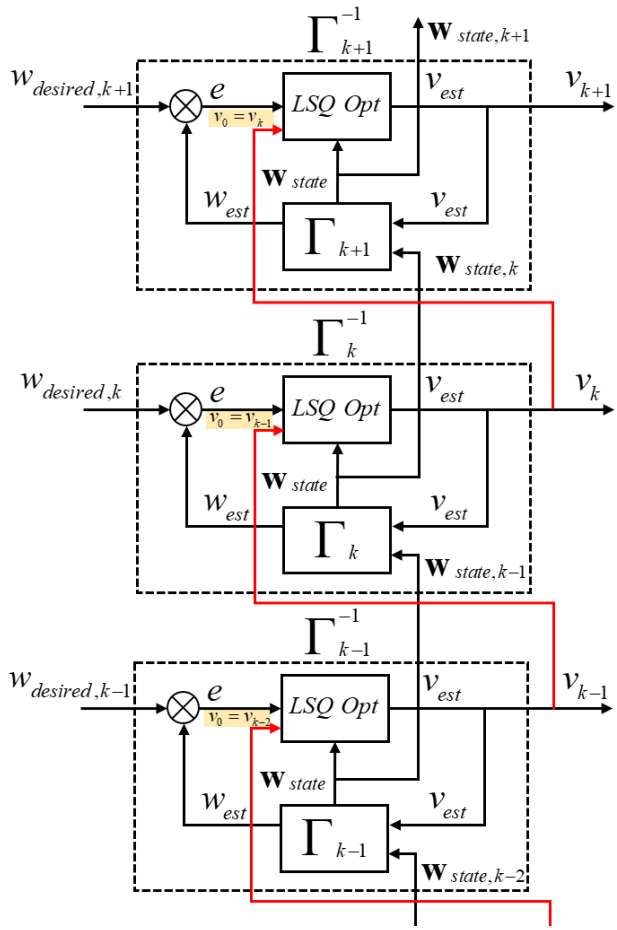


Fig. 4.32 Updating the initial value of $LSQOpt$ from the last time step output

Lastly, we must consider for the very first inversion point, that is for $k=1$. For the initial internal state, $\mathbf{W}_{state}=(0,\cdots 0)$, $v_0=0$ is a physically intuitive choice, since in actual application, the TDM will always start from a zero-input position, or a straight reference position. The final schematic of recursive inversion process is presented in Fig. 4.33.

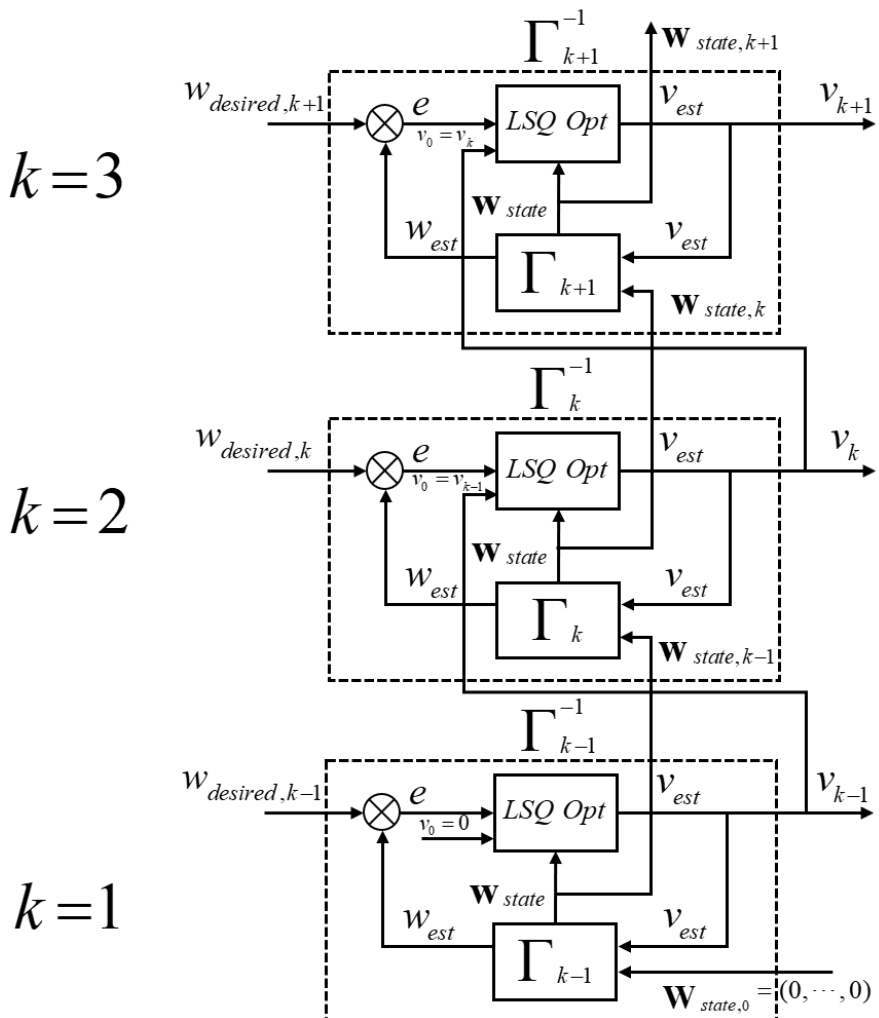


Fig. 4.33 The complete schematic of inversion procedure for $\Gamma_k^{-1}$, for time steps $k=1,2,3$. Further steps will be identical.

## 4.7 Experimental verification of hysteresis compensation with the inverse operator: $\Gamma^{-1}$

### 4.7.1. Experiment setup

For the verification of the inverse operator $\Gamma^{-1}$'s performance in compensating hysteresis, three types of desired output profiles were tested: a mixed sinusoidal profile, sinusoidal wave profile and triangular wave profile, as shown in Fig. 4.34.

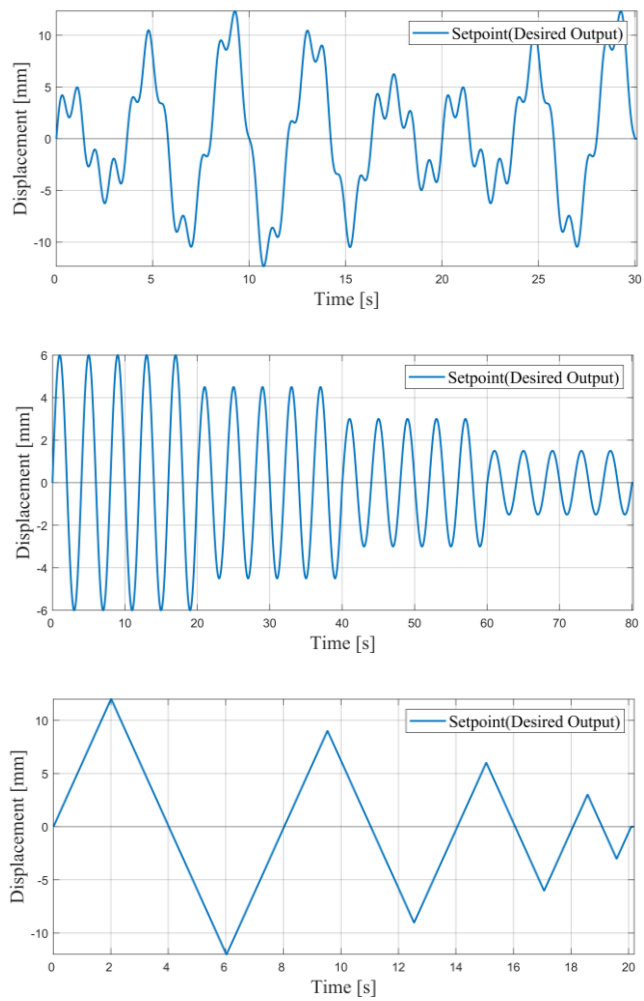


Fig. 4.34 Three types of desired output profiles: (a)mixed sinusoidal, (b)sinusoidal wave, (c)triangular wave

The sinusoidal wave profile and triangular wave profile are identical profiles used in previous sections. The mixed sinusoidal profile is a combination of sine functions with different amplitudes and frequencies, as presented below:

$$w_{desired} = 7\sin\left(\frac{1}{4}\pi t\right) + 2\sin\left(\frac{1.1}{4}\pi t\right) - 4\sin\left(\frac{0.2}{4}\pi t\right) + \sin\left(\frac{0.45}{4}\pi t\right) \qquad (4.11)$$

As for the shape configuration, two shapes out of the 24 shape configurations were selected to demonstrate the hysteresis compensation by inverse operator. The shapes are $\phi = 90^{\circ}, r = 30mm$ and $\phi = 60^{\circ}, r = 60mm$. The desired output profile is processed by respective inverse operator corresponding to the shape configuration. Then the generated input signal which compensates the hysteresis is fed as an input to the motor, and the compensated output was measured. For comparison, an output measurement from the desired output without an inverse operator process was also measured. Error statistics for each shape and desired output profiles is analyzed and will be presented in the following sections.

### 4.7.2. Result of hysteresis compensation for shape $\phi = 90°, r = 30mm$

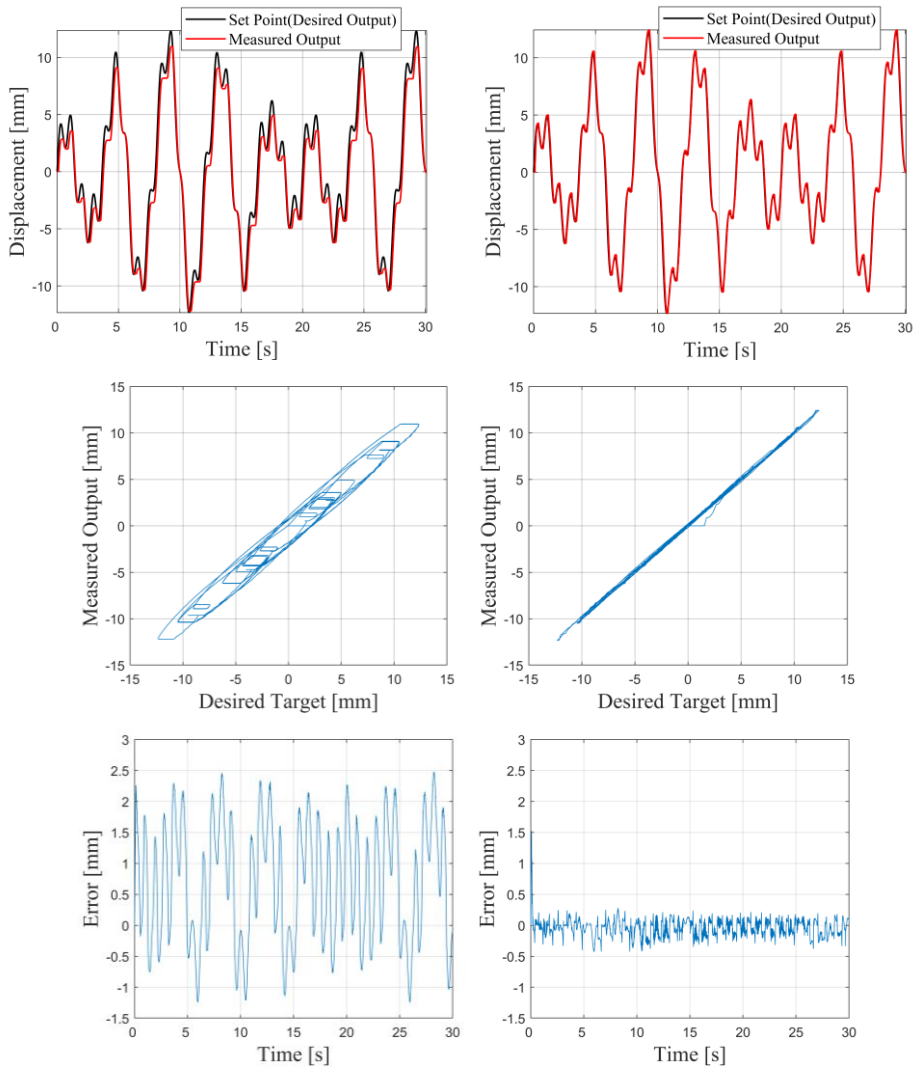


Fig. 4.35 Experiment results of hysteresis compensation with desired output setpoint of mixed sinusoidal profile at $\phi = 90^{\circ}, r = 30mm$ (left: without compensation, right: compensation with inverse operator): (a)desired setpoint and measured output. (b)input-output map, (c) error

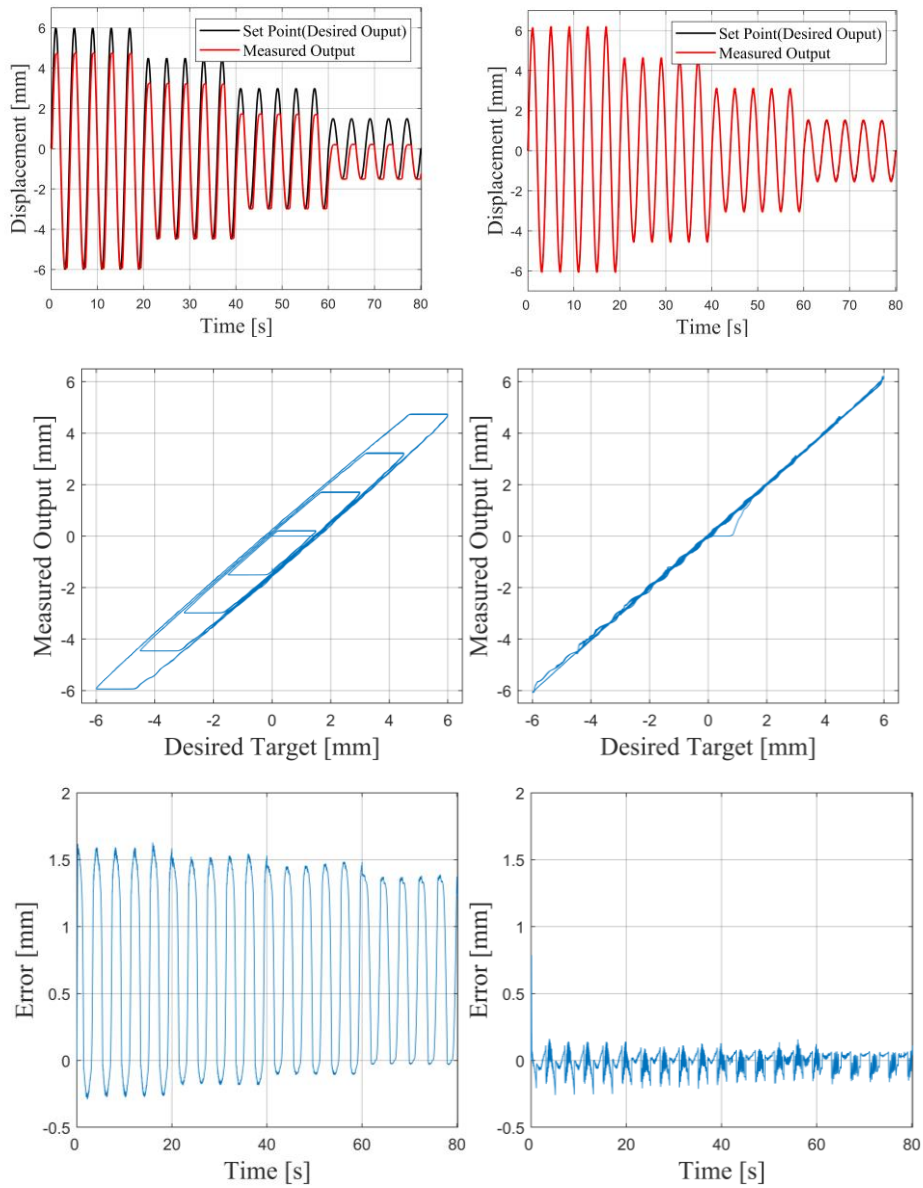


Fig. 4.36 Experiment results of hysteresis compensation with desired output setpoint of sinusoidal wave profile at $\phi = 90^{\circ}, r = 30mm$ (left: without compensation, right: compensation with inverse operator): (a)desired setpoint and measured output. (b)input-output map, (c) error

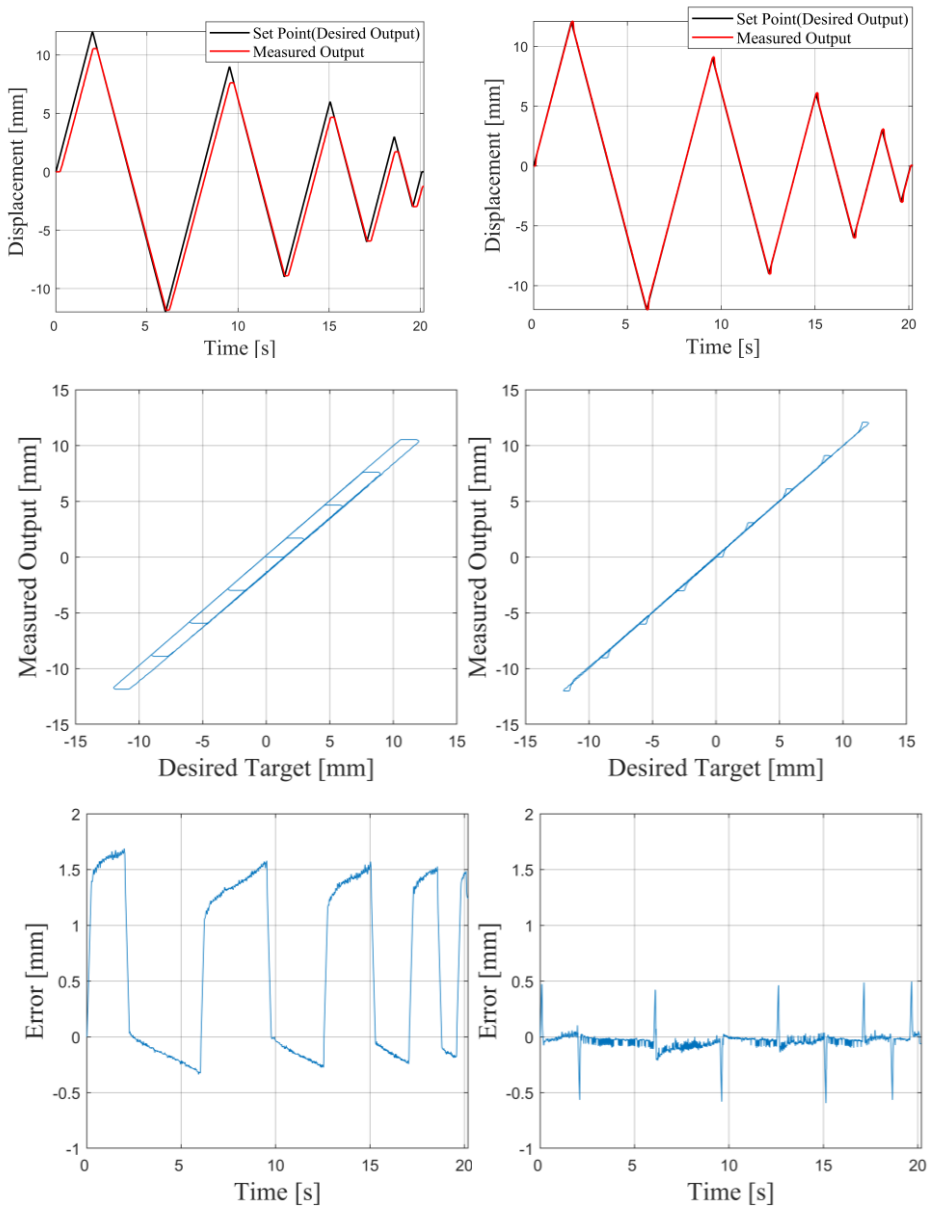


Fig. 4.37 Experiment results of hysteresis compensation with desired output setpoint of triangular wave profile at $\phi = 90^{\circ}, r = 30mm$ (left: without compensation, right: compensation with inverse operator): (a)desired setpoint and measured output. (b)input-output map, (c) error

### 4.7.3. Result of hysteresis compensation for shape $\phi = 60°, r = 60mm$

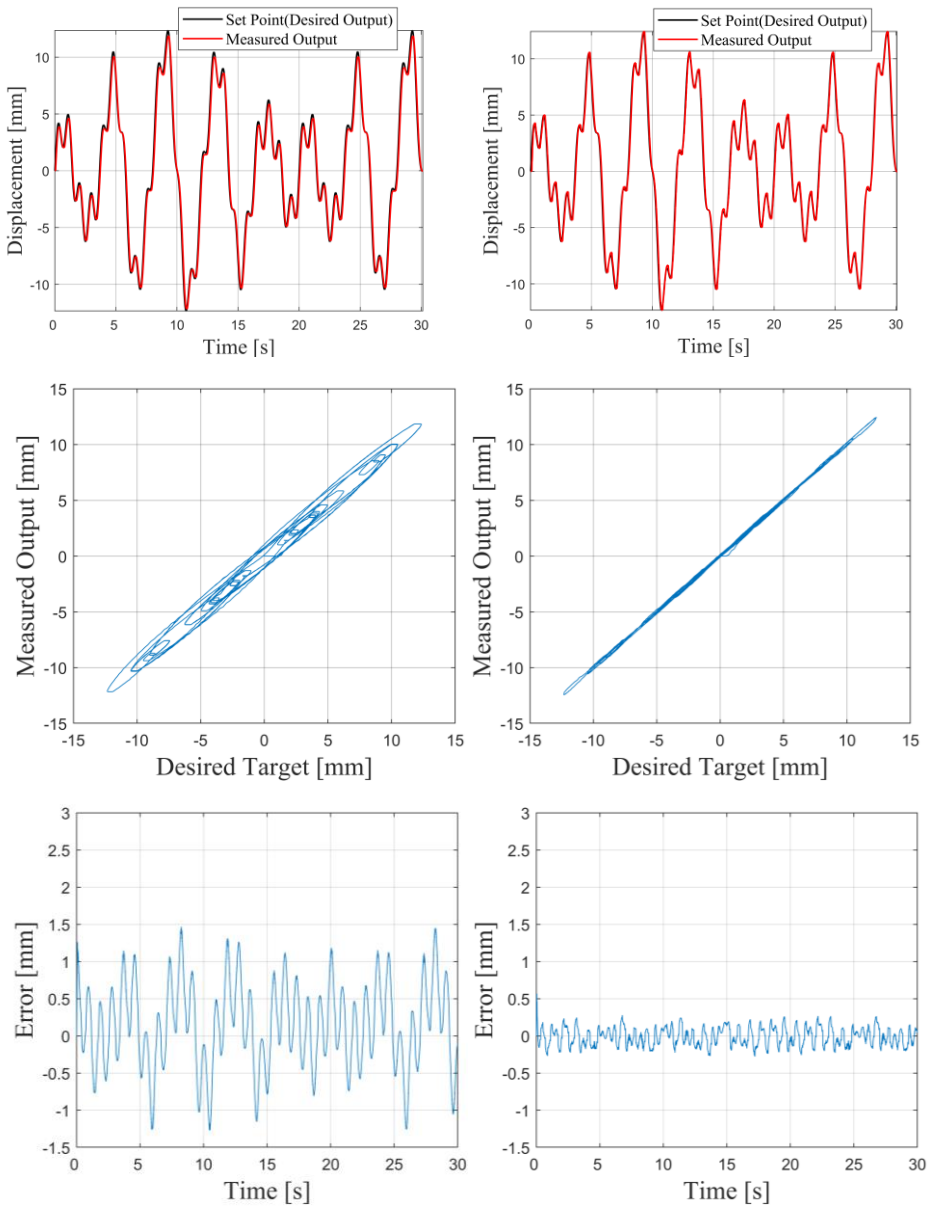


Fig. 4.38 Experiment results of hysteresis compensation with desired output setpoint of mixed sinusoidal profile at $\phi = 60^{\circ}, r = 60mm$ (left: without compensation, right: compensation with inverse operator): (a)desired setpoint and measured output. (b)input-output map, (c) error

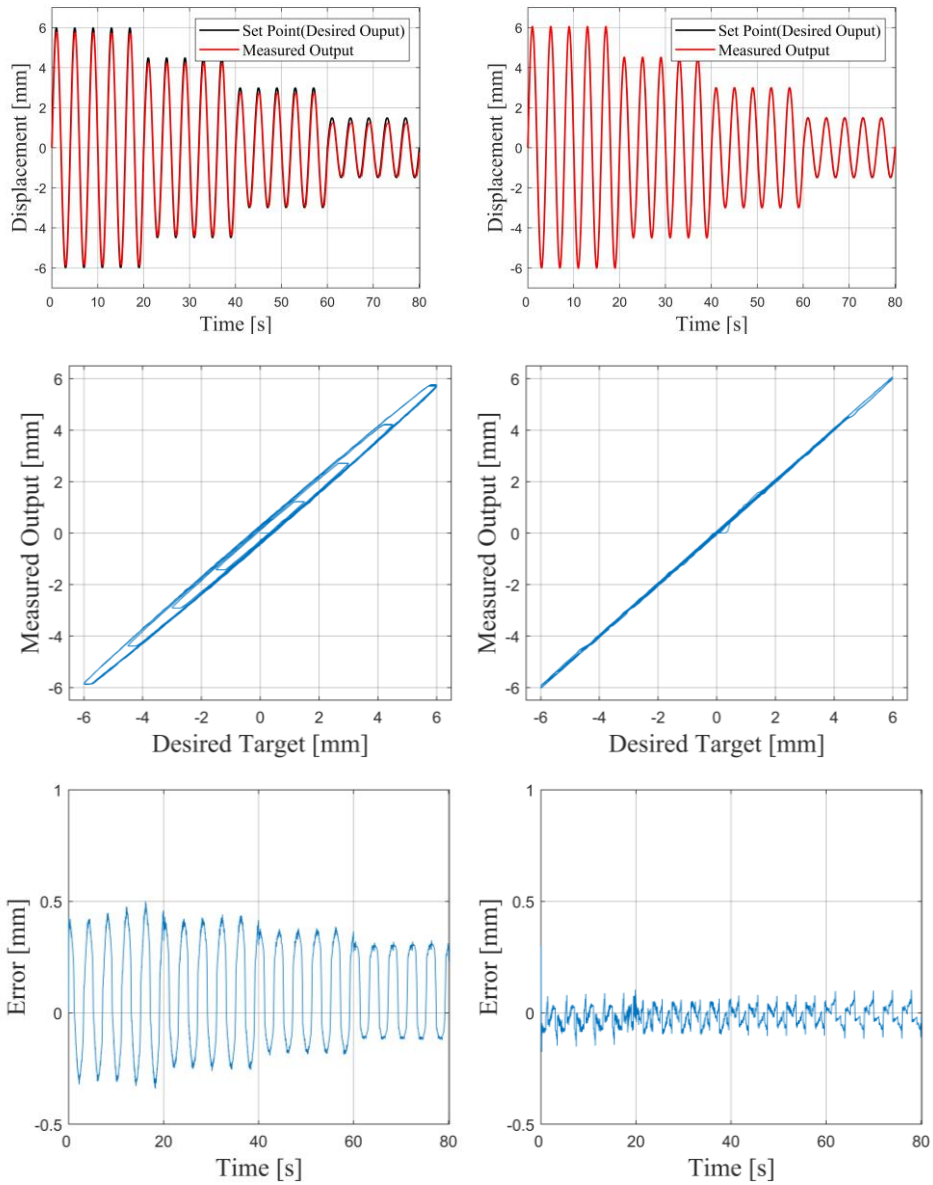


Fig. 4.39 Experiment results of hysteresis compensation with desired output setpoint of sinusoidal wave profile at $\phi = 60^{\circ}, r = 60mm$ (left: without compensation, right: compensation with inverse operator): (a)desired setpoint and measured output. (b)input-output map, (c) error

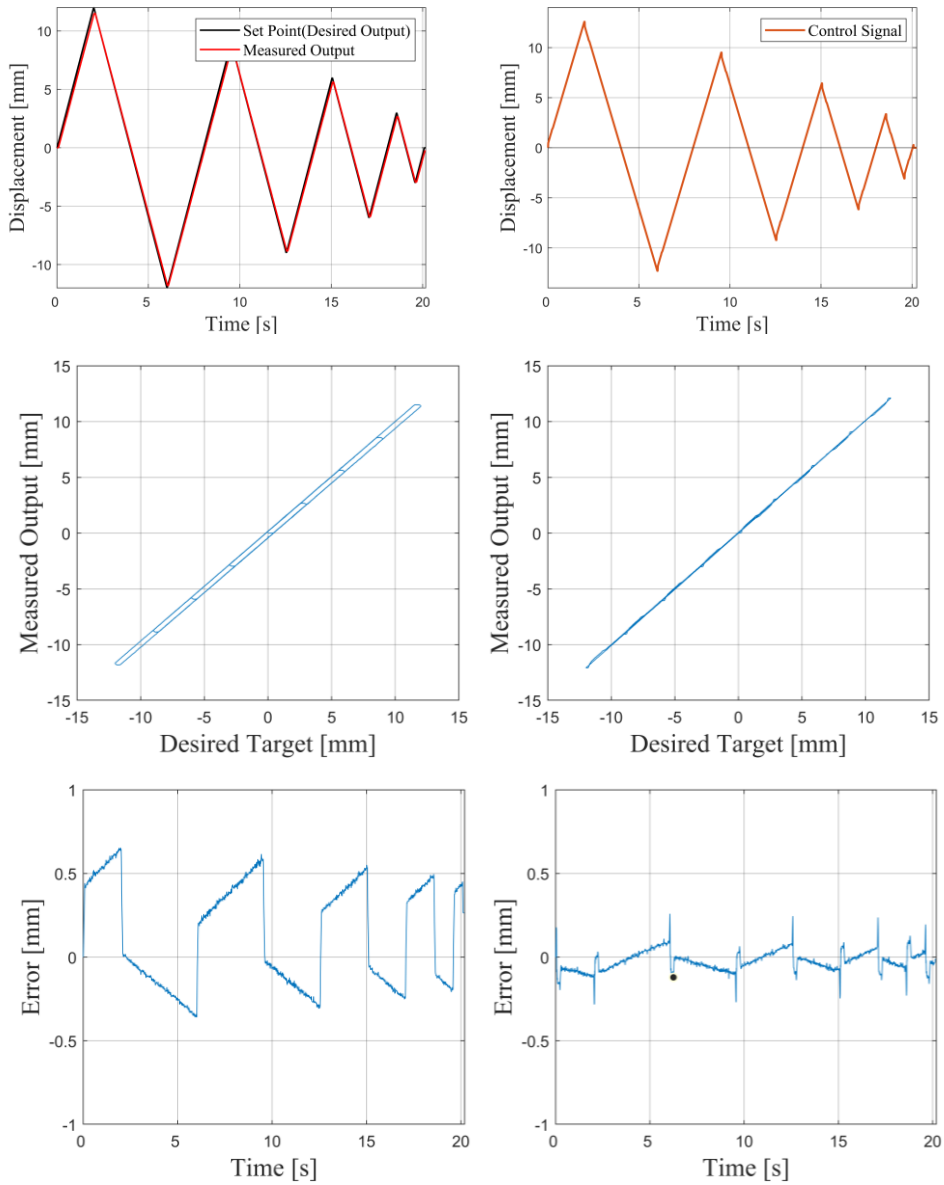


Fig. 4.40 Experiment results of hysteresis compensation with desired output setpoint of triangular wave profile at $\phi = 60^{\circ}, r = 60mm$ (left: without compensation, right: compensation with inverse operator): (a)desired setpoint and measured output. (b)input-output map, (c) error

## 4.7.4 Error statistic and result analysis

Table 4.2 summarizes the error statistics for each desired output profiles and for each shape configurations. Shape A is $\phi = 90^{\circ}, r = 30mm$ and shape B is $\phi = 60^{\circ}, r = 60mm$.

Table 4.2 Error statistics of Shape A,B for different desired output profiles

| | | **Shape A** | | **Shape B** | |
|---|---|---|---|---|---|
| **Type** | **Statistic** | No Compensation | With Compensation | No Compensation | With Compensation |
| **Mixed** | $S_{n-1}$ | 0.972 | 0.145 | 0.580 | 0.123 |
| | $\bar{e}$ | 0.688 mm | -0.041 mm | 0.144 mm | -0.009 mm |
| | $e_{max-min}$ | 3.727 mm | 1.952 mm | 2.739 mm | 0.947 mm |
| | ***RMSE*** | 65.349 | 8.250 | 32.803 | 6.790 |
| **Sinusoidal** | $S_{n-1}$ | 0.685 | 0.069 | 0.238 | 0.041 |
| | $\bar{e}$ | 0.650 mm | -0.011 mm | 0.086 mm | -0.015 mm |
| | $e_{max-min}$ | 1.919 mm | 1.045 mm | 0.841 mm | 0.475 mm |
| | ***RMSE*** | 84.564 | 6.303 | 22.601 | 3.949 |
| **Triangular** | $S_{n-1}$ | 0.765 | 0.083 | 0.307 | 0.058 |
| | $\bar{e}$ | 0.634 mm | -0.035 mm | 0.134 mm | -0.024 mm |
| | $e_{max-min}$ | 2.026 mm | 1.091 mm | 1.014 mm | 0.542 mm |
| | ***RMSE*** | 44.648 | 4.039 | 15.012 | 2.829 |

It is clear from the table that the generated inverse signal from $\Gamma^{-1}$ adequately compensates the hysteresis of TSM. One thing to note from the error statistics is that the mean of error $\bar{e}$, is always negative for the compensated result. This is due to the fact that when the weights $\mathbf{Q}$, of forward hysteresis operator is obtained through optimization, the $\mathbf{QQ^T}$ condition which constrains the sum of all weights to 1, forces the optimizer to end loop before the sum reaches 1. Another point that needs

to be addressed is the $e_{\max-\min}$ which, compared to other statistics, does not show equivalent amount of improvement. This is due to the fact that there is always a phase delay when the desired output is first fed to the inversion algorithm. The delay causes a peak error at the initial portion of the desired output profile as can be seen in Fig. 4.34 through Fig. 4.39.

One of the main objectives of this research was implementing a hysteresis compensation scheme that is fast and realizable in real time processing. Table 4.3 summarizes the calculation time of one time step when using different algorithms for the $LSQOpt$ portion of the inversion process. The three algorithms that are compared are Nelder-Mead Simplex Method, Interior-Point Algorithm and Golden Section Search, Parabolic Interpolation, which are implemented in a function forms as FMINSEARCH, FMINCON and FMINBND, respectively, in Matlab.

Table 4.4 Average calculation time for different algorithms of $LSQOpt$

| | Shape A | | | Shape B | | |
|---|---|---|---|---|---|---|
| | FMINSEARCH | FMINCON | FMINBND | FMINSEARCH | FMINCON | FMINBND |
| **Mixed** | 161.23ms | 33.97ms | 0.48ms | 149.42ms | 32.96ms | 0.40ms |
| **Sinusoidal** | 144.81ms | 27.02ms | 0.34ms | 112.97ms | 26.12ms | 0.38ms |
| **Triangular** | 138.71ms | 34.22ms | 0.40ms | 129.48ms | 34.67ms | 0.38ms |

The average calculation time is a time to reach $v_k$ from a given desired $w_{desired,k}$ at time step $k$. The specifications of the desktop system that produced such results were I7-8700K at 4.1GHz, 32GB RAM, with the Matlab R2018B environment. Consequently we can arrive at a conclusion that with the desktop system that generated the inverse control signal, the FMINBND algorithm (Golden Section Search, Parabolic Interpolation) would be more than enough to realize a real-time

compensation scheme. Utilizing the controller used for such experiment setup (cRIO-9082), which is equipped with a FPGA, FMINCON may also be a candidate for real-time application when implemented under FPGA, considering the fact that FPGA is unrivaled in computation time when compared to the conventional desktop system operating under Windows OS.

# Chapter 6. Conclusion

The need for tendon-sheath mechanism (TSM) coincides with the evolutionary trend of surgical robotics heading towards flexible surgical platforms.

Though regarded as an only feasible solution for implementing flexible surgical instruments, due to its structure TSM exhibits hysteretic behavior.

Previous studies focused on reporting such degradation of performance of TSM, and attempts were made to compensate for the hysteretic output. But many proposed methods have setbacks that are inapplicable in implementing a robust compensation scheme in terms of position control.

In this research, there are three stages of experiment towards constructing a robust hysteresis compensation strategy when the shape of TSM is varied. The first stage of experiment was a series of observations on TSM's hysteretic output varying in accordance with the defined shape parameters.

A Preisach-type discretized model based on mechanical play operators were proposed and its feasibility was verified with the second stage of experiments.

A fast and accurate inversion strategy is essential in compensating for hysteresis in real time. An inversion scheme was developed and was verified with the third stage of experiments. The accuracy of the inversion operator and calculation time for each step of the inversion process were measured and presented, concluding with a fact that such model is feasible for use in real-time for compensation of hysteresis in TSM.

# Bibliography


[1] Y. Kwoh, J. Hou, E. Jonckheere and S. Hayati, "A robot with improved absolute positioning accuracy for CT guided stereotactic brain surgery.," *IEEE Transactions on Biomedical Engineering,* no. 35, pp. 153-160, 1988.

[2] M. Marino, G. Shabat and G. Gulotta, "From Illusion to Reality: A Brief History of Robotic Surgery," *Surgical Innovation,* vol. 25, no. 3, pp. 291-296, 2018.

[3] R. Santava, "Robotic surgery: from past to future- a personal journey," *Surgical Clinics of North America,* vol. 83, pp. 1491-1500, 2003.

[4] J. Bowersox, "Telepresence surgery," *British Journal of Surgery,* vol. 83, pp. 433-444, 1996.

[5] S. Unger, H. Unger and RT.Bass, "AESOP robotic arm," *Surgical Endoscopy,* vol. 8, p. 1131, 1994.

[6] Maxon Group, "Surgical Robots for Minimally Invasive Procedures," 2010. [Online]. Available: http://www.maxongroup.com/maxon/view/application /SURGICAL-ROBOTS-AB. [Accessed August 2020].

[7] B. Challacombe, S. Khan and D. Murphy, "The history of robotics in urology," *World Journal of Urology,* p. 120, 2006.

[8] T. Lane, "A short history of robotic surgery," *Annals of The Royal College of Surgeons of England,* vol. 100, no. 6, pp. 5-7, 2018.

[9] Intuitive Surgical Inc., "Da Vinci SP," [Online]. Available: http://www.intuitive.com/en-us/products-and-services/da-vinci/systems. [Accessed August 2020].

[10] University of Basel, "Flexible Robotic Endoscope," [Online]. Available: https://dbe.unibas.ch/en/research/laser-and-robotics/bio-inspired-robots-for-medicine-lab/articulated-flexible-endoscope/. [Accessed August 2020].

[11] J. Lee, J. Kim, K. Lee, S. Hyung, Y. Kim, W. Kwon, K. Roh and J. Choi, "Modeling and Control of Robotic Surgical Platform for Single-Port Access Surgery," in *IEEE/RSJ International Conference on Intellifent Robots and Systems*, Chicago, 2014.

[12] Medrobotics, "Flex Robotic System: Expanding the reach of surgery," [Online]. Available: http://medrobotics.com/gateway/flex-robotic-system/. [Accessed August 2020].

[13] T. Do, T. Tjahjowidodo, M. Lau and S. Phee, "A new approach of friction model for tendon-sheath actuated surgical systems: Nonlinear modelling and parameter identification," *Mechanism and Machine Theory,* vol. 85, pp. 14-24, 2015.

[14] S. Phee, S. Low, V. Huynh, A. Kencana, Z. Sun and K. Yang, "Master and slave transluminal endoscopic robot (MASTER) for Natural Orifice Transluminal Endoscopic Surgery (NOTES)," in *Annual international conference of the IEEE engineeding in medicine and biology society*, 2009.

[15] B. Bardou, F. Nageotte, P. Zanne and M. d. Mathelin, "Impovements in the control of a flexible endoscopic system," in *IEEE international conference on robotics and automation (ICRA)*, 2012.

[16] D. Abbot, C. Becke and W. P. RI. Rothstein, "Design of an endoluminal NOTES robotic system," in *IEEE/RSJ international conference on intelligent robots and systems*, 2007.

[17] G. Dachs and W. Peine, "A novel surgical robot design: Minimizing the operating envelope within the sterile field," in *Annual international conference of the IEEE engineering in medicine and biology society*, 2006.

[18] T. Cooper, C. Julian, S. Blumenkranz and R. Younge, "Mechanical actuator interface system for robotic surgical tools". United States of America Patent US6491701, 10 December 2002.

[19] T. Do, T. Tjahjowidodo, M. Lau, T. Yamamoto and S. Phee, "Hysteresis modeling and position control of tendon-sheath mechanism in flexible endoscopic systems," *Mechatronocs,* vol. 24, no. 1, pp. 12-22, 2014.

[20] M. Kaneko, T. Tamashita and K. Tanie, "Basic considerations on transmission characteristics for tendon drive robots," in *International Conference on Advanced Robotics (ICAR),'Robots in Unstructured Environments'*, 1991.

[21] M. Kaneko, M. Wada, H. Maekawa and K. Tanie, "A new consideration on tendon-tension control system of robot hands," in *IEEE International Conference of Robotics and Automation (ICRA)*, 1991.

[22] Carl Stahl Sava Industries, "Push-Pull Components," [Online]. Available: http://www.savacable.com/push-pull-components. [Accessed August 2020].

[23] G. Palli and C. Melchiorri, "Model and control of tendon-sheath transmission systems," in *IEEE international conference on robotics and automation (ICRA)*, 2006.

[24] G. Palli and C. Melchiorri, "Optimal control of tendon-sheath transmission systems," in *International IFAC sumposium on robot control*, 2006.

[25] V. Agrawal, W. Peine and B. Yao, "Modeling of a closed loop cable-conduit transmission system," in *IEEE international conference on robotics and automation (ICRA)*, 2008.

[26] V. Agrawal, W. Peine and B. Yao, "Modeling of transmission characteristics across a cable-conduit system," *IEEE Transactions on Robotics,* vol. 26, pp. 914-924, 2010.

[27] Asahi-Intecc, "Asahi Intecc Medical Components - Products," [Online]. Available: https://components.asahi-intecc.com/us/products/coils. [Accessed 29 5 2020].

[28] Carl Stahl Sava Industries, "Basic Wire Rope Construction," [Online]. Available: http://www.savacable.com/cable-information#construction. [Accessed 20 5 2020].

[29] Asahi-Intecc, "Product Lineup," [Online]. Available: http://components.asahi-intecc.com/storage/app/media/product_catalogs /cable_catalogue. [Accessed 20 5 2020].

[30] A. Visintin, Differential Models of Hysteresis, Berlin: Springer, 1994.

[31] I. Mayergoyz, Mathematical Models of Hysteresis, New York: Sprinder-Verlag, 1991.

[32] F. Tian and X. Wang, "The design of a tendon-sheath-driven robot," in *International conference on mechatronics and machine vision in practice*, 2008.

[33] S. Low, S. Phee, P. Valdastri, A. Menciassi and P. Dario, "Tendon sheath anlysis for estimation of distal end force and elongation," in *IEEE/ASME international conference on advanced intelligent mechatronics (AIM)*, 2009.

[34] S. Kesner and R. Howe, "Design and control of motion compensation cardiac

catheters," in *IEEE international conference on robotics and automation (ICRA)*, 2010.

[35] S. Kesner and R. Howe, "Position control of motion compensation cardiac catheters," *IEEE Transactions on Robotics,* vol. 27, pp. 1045-1055, 2011.

# Abstract

본 연구에서는 유연한 로봇 수술도구를 구현하기 위해 사용되는 Tendon-Sheath Mechanism (TSM)이 형상에 따른 이력현상의 변화가 발생하는 것을 실험적으로 확인하였으며, 이러한 이력현상을 표현하기 위한 모형을 제안하고 이를 이용하여 이력현상을 보상할 수 있는 알고리즘을 제안하였다.

첫 단계로 TSM을 구성하는 부품인 Tendon과 Sheath를 선정하는데 있어, 이력현상에 일조 하는 비선형적 특성을 최소화하는 재료와 공정 및 후처리 방법을 고려하여 적용하였다. 다음으로 TSM의 형상 변수를 정의하고 이를 다양한 형상하에서 이력현상의 변화를 관찰하는 실험장치를 설계하여 실험 데이터를 수집하였다. 이를 토대로 입력에 대한 출력의 관계를 Preisach type 연산자를 이용하여 표현하였고 실험 데이터에 기반한 연산자의 변수들을 최소자승 최적화를 통해 탐색하였으며, 모델의 적합성을 다양한 형상하에서, 각기 다른 종류의 입력 신호에 대한 출력을 모델을 통해 생성되는 출력 추정치와의 오차 분석으로 검증하였다.

이러한 모델로 이력현상을 보상하기 위해서 Set-Point 출력에 대한 Inverse Control 신호를 생성하는 재귀적 알고리즘을 제안하였으며, 이러한 알고리즘이 다양한 Set-point 출력의 형태에 대해서 실시간성이 보장되는 빠른 연산이 가능하다는 점을 보였다. 이력현상이 보상된 실험데이터와 기존의 보상전 실험데이터의 비교를 통해 보상전략이 효과적이라는 것을 보였으며, 다양한 형태에서도 적용이 가능함을 검증하였다.

**주요어** : 수술로봇, 로봇수술도구, 유연구동 메커니즘, 이력현상모형, 위치제어

**학번** : 2015-30165